AN ABSTRACT OF THE THESIS OF

Kellen Charles Doyle for the degree of Master of Science in Civil Engineering presented on March 13, 2024.

Title: Laboratory Observations of Tsunami-Driven Debris Damming with Comparison to ASCE 7-22 Minimum Design Loads

Abstract approved: _____

Daniel T. Cox

Tsunami inundation of coastal communities can impose a wide array of forces on the built environment. Forces generated by tsunami-driven debris damming have the potential to cause failure of coastal structures and further accumulate flow-entrained debris. Since tsunami-resilient design standards were adopted by ASCE in 2016, debris damming considerations have not been thoroughly evaluated in comparison to physical model studies.

Much existing debris damming literature comes from hydraulic engineering in which steady flow conditions are commonly used. Recent laboratory experiments have shifted towards unsteady, transient flow modelling, however most use small-scale debris and limited flume widths relative to the structural specimen. It remains unclear how steady flow results can be translated to coastal engineering applications and how debris damming load estimates in current structural standards compare to experimentally observed forces. As such, the purpose of this thesis is to compare current ASCE 7-22 load prediction components to experimental debris damming results.

This experiment was performed in the Large Wave Flume of the O.H. Hinsdale Wave Research Laboratory at Oregon State University. Incident waves propagated as a tsunami-like bore over a flat wet-bed test section, entraining debris elements from a debris source platform and freely accumulating these elements against a column array representing an elevated coastal structure. Two different lengths of 1:20 geometric scaled shipping containers were considered in this study and three different column densities were modelled, representing both Open and Closed structures per ASCE 7-22 definitions. In addition to horizontal debris damming loads,

submerged projected areas of in-situ experimental debris dams were analyzed via a new photogrammetric method for comparison to minimum closure ratios proposed in ASCE 7-22.

Results of this study indicate that two alternative methods of tsunami horizontal load prediction may yield widely varying levels of structural design conservatism. ASCE 7-22 Equation 6.10-1, a simplified equivalent uniform lateral static pressure approach, yields reasonable design factors of safety for high Froude ($Fr > 0.8$) regime inundation, but becomes overconservative and likely impractical for design under lower velocity flows. Conversely, ASCE 7-22 Equation 6.10-2, a detailed hydrodynamic lateral force approach, is often unconservative and seems to be exacerbated by high Froude ($Fr > 0.8$) regime inundation and larger debris elements. However, this approach does seem reasonable for design for dense column configurations under low Froude ($Fr < 0.7$) regime inundation.

Assumed minimum closure ratios due to debris accumulation and overall structure drag coefficients both serve as inputs to the load prediction methods described above. Results indicate that for closed structures, the assumed minimum closure ratio of 0.7 is conservative under almost all tested conditions. The assumed minimum closure ratio for open structures of 0.5 is often unconservative and is exceeded under all three incident wave conditions. This under-conservatism is also exacerbated by large debris elements.

Finally, results indicate that ASCE 7-22 drag coefficients for rectilinear structures may not capture free-surface effects and intercolumn interactions induced by flow around and through elevated coastal structures. For this reason, recent tsunami literature has adopted the use of "resistance coefficient" to capture both form drag and unbalanced hydrostatic force components. It was found that experimental resistance coefficients exceed ASCE 7-22 drag coefficients for rectilinear structures for all tested column configurations. It is proposed that a bulk resistance coefficient – intended to capture form drag and free surface effects as well as intercolumn flow interaction – may provide an improved dimensionless measure of flow resistance for surface-piercing column arrays.

Laboratory Observations of Tsunami-Driven Debris Damming with Comparison to ASCE 7-22 Minimum Design Loads

by
Kellen Charles Doyle

A THESIS

submitted to

Oregon State University

in partial fulfillment of
the requirements for the
degree of

Master of Science

Presented March 13, 2024
Commencement June 2024

Master of Science thesis of Kellen Charles Doyle presented on March 13, 2024.

APPROVED:

Major Professor, representing Civil Engineering

Head of the School of Civil and Construction Engineering

Dean of the Graduate School

I understand that my thesis will become part of the permanent collection of Oregon State University libraries. My signature below authorizes release of my thesis to any reader upon request.

Kellen Charles Doyle, Author

ACKNOWLEDGEMENTS

I would like to acknowledge all that made this thesis possible throughout my time at Oregon State University. This research campaign was funded by the National Science Foundation (NSF) Division of Civil, Mechanical, and Manufacturing Innovation (CMMI) and Natural Hazards Engineering Research Infrastructure (NHERI) through Grants #2203131, #2203116, and #2037914.

I would like to thank the staff and student employees of the O.H. Hinsdale Wave Research Laboratory (HWRL) for their help during testing and data collection as well as the CEOAS Machine and Technical Development (CMTD) facility for manufacturing of the column array specimen. Additionally, I would like to thank all members of the collaborative research team that contributed to this project including: Daniel Cox and Pedro Lomonaco (OSU), Hyoungsu Park and Myung-Jin Koh (UH), and Sabarethinam Kameshwar and Ravindu Jayasekara (LSU).

Finally, I would like to thank my family and friends both here in Oregon and back on the east coast for all their support in getting to this point. Special thanks to my parents: Brian Doyle, Emily Sevigny, Kerri Dexter, and Steve Dexter; and to my partner, Meagan Collins, for all of their support, despite the distance, throughout my time here in Oregon.

CONTRIBUTION OF AUTHORS

This research is part of a multi-year collaborative experimental campaign with contributors from Oregon State University (OSU), the University of Hawaii at Manoa (UH), and Louisiana State University (LSU). As such, the following individuals contributed throughout this first phase of the study:

Dr. Daniel Cox (OSU) as a professor served as academic advisor since September 2022 and contributed to experimental design and setup, interpretation of data, and manuscript editing.

Dr. Pedro Lomonaco (OSU), as the director of the O.H. Hinsdale Wave Research Laboratory (HWRL), contributed to experimental design and setup, collection and interpretation of data, and manuscript editing.

Dr. Hyoungsu Park (UH), as an associate professor and co-PI of the experimental campaign, contributed to experimental design and setup, interpretation of data, and manuscript editing.

Dr. Sabarethinam Kameshwar (LSU) as an associate professor and co-PI of the experimental campaign, contributed to experimental design and setup, interpretation of data, and manuscript editing.

Myung-Jin Koh (UH) as a graduate student contributed to experimental design and setup as well as collection, processing, and interpretation of data.

Ravindu Jayasekara (LSU) as a graduate student contributed to experimental design and setup as well as collection and interpretation of data.

TABLE OF CONTENTS

Page

1 Introduction 1

2 Tsunami Debris Damming Forces and Associated Coefficients for Elevated Coastal Structure Columns: Experimental Comparison to ASCE 7-22 Minimum Design Loads 4

2.1 Abstract 4

2.2 Practical Applications 4

2.3 Introduction 5

2.4 Background 7

2.4.1 Debris Damming Experiments 7

2.4.2 Resistance Coefficient of Surface-Piercing Flow Obstructions 8

2.4.3 Adoption of Tsunami-Resilient Design Standards 9

2.5 Experimental Setup 12

2.5.1 Wave Flume and Incident Wave Conditions 12

2.5.2 Column Specimen and Debris Elements 15

2.5.3 Instrumentation 16

2.6 Methods 18

2.6.1 Experimental Procedure 18

2.6.2 Photogrammetry Analysis 19

2.7 Analysis 22

2.8 Discussion 27

2.9 Conclusions 29

2.10 Data Availability Statement 30

2.11 Acknowledgements 30

2.12 References 30

TABLE OF CONTENTS (Continued)

Page

3 Conclusions 34

Bibliography 36

Appendices 40

LIST OF FIGURES

Figure Page

2.1 LWF experimental setup at HWRL 12

2.2 Annotated photo of LWF experimental setup 13

2.3 Wavemaker displacement during ERF wave generation 14

2.4 Mid-specimen (a) free surface displacement relative to flat test section elevation and (b) flow velocity 15

2.5 Schematic of column array specimen dimensions 16

2.6 Initial debris element configuration on debris platform and inundation flow direction 18

2.7 Example experimental trial (Wave C, 6.1 m SC, 3x7 column array) 19

2.8 Example FBP time-series 20

2.9 Debris dam test case projected area calculation for photogrammetry method validation 21

2.10 Results of photogrammetric method validation campaign 22

2.11 Comparison of experimental debris damming forces to ASCE 7-22 Section 6.10 Equations 6.10-1 and 6.10-2 23

2.12 Comparison of experimental closure ratios to ASCE 7-22 Section 6.8.7 minimum closure ratios 25

2.13 Comparison of experimental bulk resistance coefficients to ASCE 7-22 Table 6.10-1 drag coefficients for rectilinear structures 26

LIST OF TABLES

Table		Page
2.1	Error function-generated incident wave hydrodynamic conditions at midpoint of column array	14
2.2	Experimental column array configurations	15
2.3	Hydrodynamic instrumentation layout relative to LWF coordinate space	17
2.4	Summary of photogrammetric method validation results	22
2.5	Hydrodynamic bulk resistance coefficient statistics of each column configuration	26

LIST OF APPENDICES

Appendix		Page
A.	Incident Wave Conditions	41
B.	Debris Element Catalog	44
C.	Photogrammetry Archetypes	47
D.	Photogrammetry Method Validation and Error Analysis	49
E.	Analyzed Experimental Debris Dams	51

LIST OF APPENDIX FIGURES

Figure Page

A.1 Free-surface elevations as measured by resistance wave gauges (wg).....41

A.2 Free-surface elevations as measured by ultrasonic wave gauges (uswg) 42

A.3 Flow velocities as measured by acoustic doppler velocimeters (adv) 43

A.4 Fabrication specification of 1:20-scale 6.1 m (20 ft) shipping container debris elements 46

A.5 Fabrication specification of 1:20-scale 12.2 m (40 ft) shipping container debris elements 46

A.6 Archetype images for 6.1 m (20 ft) shipping containers 47

A.7 Archetype images for 12.2 m (40 ft) shipping containers 48

A.8 Example photogrammetry method validation test case 49

A.9 Error quantification of CAD-based test case measurement.....50

LIST OF APPENDIX TABLES

Table Page

A.1 Inventory of 1:20-scale 6.1 m (20 ft) shipping container debris elements 44

A.2 Inventory of 1:20-scale 12.2 m (40 ft) shipping container debris elements 45

A.3 Summary of analyzed experimental debris dam test parameters.....51

A.4 Summary of analyzed experimental debris dam hydrodynamic values 55

A.5 Summary of analyzed experimental debris dam results 59

DEDICATION

This thesis is dedicated to my great grandfather, Charles Kennedy, former head of Water Resources for the State of Massachusetts and the original civil engineer in the family.

1. Introduction

Overland flow during coastal inundation events poses major hazards to coastal communities worldwide. As these coastal communities continue to grow in population and development, the severity of these hazards will only increase. Effects of entrained debris during both hurricane surge and tsunami overland flow can be a critical load case (Robertson et al. 2007; Stolle et al. 2020) as debris impacts and/or accumulates against a coastal structure.

This thesis work is part of a multi-year collaborative experimental campaign involving the University of Hawaii (UH), Louisiana State University (LSU), and Oregon State University (OSU) to investigate tsunami-driven debris damming effects on coastal structures. Lead principal investigators of this campaign are Dr. Hyoungsu Park (UH) and Dr. Sabarethinam Kameshwar (LSU). Physical experiments are being performed in two phases in the Large Wave Flume (LWF) at the O.H. Hinsdale Wave Research Laboratory (HWRL) at OSU, with collaboration from Dr. Pedro Lomonaco and Dr. Daniel Cox. The main goals of the experimental campaign are to investigate (1) the mechanisms that lead to debris damming during tsunamis, (2) the factors that increase structural loading due to debris damming, and (3) the effects of non-homogeneous debris on resulting debris dams and loads. The work presented herein represents a contribution to the experimental campaign using data from the first phase of physical experimentation, performed February through May 2023.

A number of recent tsunamis – Indian Ocean earthquake and tsunami (2004), Samoan earthquake and tsunami (2009), Chilean earthquake and tsunami (2010), Tohoku tsunami (2011), and Sulawesi earthquake and tsunami (2018) – have underscored the importance of accurate tsunami-resilient structural design standards. ASCE 7-22 Chapter 6: Tsunami Loads and Effects represents “the first national, consensus-based standard for tsunami resilience” (Chock 2016; ASCE 2020) and provides design methodology for vertical evacuation refuge structures (VERS) in coastal communities where access to natural high ground is limited by distance or evacuation time.

While ASCE 7-22 debris impact considerations have been thoroughly studied in physical model experiments, debris damming has yet to be as thoroughly reviewed. Some recent work has begun to bridge the gap between earlier hydraulic engineering debris damming studies to tsunami-driven debris damming (Stolle et al. 2018; Wütrich et al. 2019; Shekhar et al. 2020). While beneficial to understanding debris damming likelihood and mechanisms, none have

compared back to the debris damming-induced hydrodynamic design loads prescribed in ASCE 7-22.

This work compares experimental debris damming results to values outlined in ASCE 7-22, specifically lateral force-resisting system design loads, closure ratio due to debris accumulation, and overall structure drag coefficients. A new photogrammetric method for assessing in-situ debris dams is validated and implemented and an alternative resistance coefficient is explored in terms of surface-piercing structural column arrays.

The second phase of physical experimentation (scheduled for Fall 2024) and ongoing data analysis is expected to further elucidate tsunami-driven debris damming mechanisms and forces. Anticipated publications and presentations regarding this experimental campaign are included in Chapter 3: Conclusions.

TSUNAMI DEBRIS DAMMING FORCES AND ASSOCIATED COEFFICIENTS FOR ELEVATED COASTAL STRUCTURE COLUMNS: EXPERIMENTAL COMPARISON TO ASCE 7-22 MINIMUM DESIGN LOADS

Kellen Doyle

Myung-Jin Koh

Ravindu Jayasekara

Daniel Cox

Hyoungsu Park

Sabarethinam Kameshwar

Pedro Lomonaco

American Society of Civil Engineers

Journal of Structural Engineering

1801 Alexander Bell Drive

Reston, VA 20191-4400

Submitted February 12, 2024

2. Tsunami Debris Damming Forces and Associated Coefficients for Elevated Coastal Structure Columns: Experimental Comparison to ASCE 7-22 Minimum Design Loads

2.1 Abstract

Debris damming forces of 1:20-scale shipping containers freely accumulated against elevated coastal structure columns were experimentally determined to evaluate ASCE 7-22 tsunami-resilient design standards. Three inundation conditions were generated to represent Froude regimes estimated in post-tsunami field studies. Three different column array densities and two different shipping container sizes were evaluated. A photogrammetric method was employed to estimate the submerged projected area of in-situ transient debris dams from two synchronized camera perspectives. Relative to this experimental data, it was found that the ASCE 7-22 equation for simplified equivalent uniform lateral static pressure (Eq. 2) is conservative by as much as 6.9 times the measured horizontal forces generated by debris damming. Conversely, the ASCE 7-22 equation for detailed hydrodynamic lateral forces (Eq. 3) is often unconservative and is exacerbated by near-critical Froude regime inundation flows and large debris elements. Minimum closure ratios and overall structure drag coefficients serve as input values for these hydrodynamic lateral design loads. Minimum closure ratios for load determination per ASCE 7-22 Section 6.8.7 tend to be fairly conservative for closed structures, however unconservative for open structures with sparser column densities. Finally, drag coefficients for rectilinear structures per ASCE 7-22 Table 6.10-1 appear unrepresentative of elevated coastal structures, which tend to generate column-flow interactions and unbalanced hydrostatic conditions. It is therefore suggested that flow resistance of such structures be quantified via a bulk resistance coefficient, indicated by recent literature as a more appropriate measure applicable to surface-piercing flow obstructions.

2.2 Practical Applications

Since the 2016 adoption of tsunami-resilient design standards in ASCE 7-16, debris damming design loads have yet to be thoroughly examined. The results of this experiment indicate that the application of hydrodynamic loading equations in ASCE 7-22 Section 6.10 may have significant influence on the factor of safety of the lateral-force-resisting system of a structure. This finding has the potential to drastically impact design conservatism. Debris

accumulation on the seaward face of open structures often exceeds the minimum closure ratio for load determination, however the minimum closure ratio for closed structures appears conservative relative to the experimental data. Finally, drag coefficients for rectilinear structures may not capture phenomena associated with surface-piercing flow obstructions such as column-flow interactions and unbalanced hydrostatic forces. It is suggested that bulk resistance coefficient be adopted to account for both form drag and surface effects of flow around elevated coastal structure columns. Accurate quantification of tsunami-induced loads is crucial to the design of critical and essential infrastructure located within tsunami inundation zones, especially vertical evacuation refuge structures.

2.3 Introduction

Tsunami overland flow in coastal areas has the potential to induce widespread debris effects on the built environment, including phases of debris entrainment, transport, impact, and damming. An emphasis on understanding these processes in the context of structural loading and failure modes has grown in recent years following a number of extreme tsunami events (Nistor et al. 2017).

Post-event field studies often highlight the variability of debris types and source locations during coastal inundation. Hurricane Katrina, generating similar damage to that of the 2004 Indian Ocean tsunami, showed that “any floating or mobile object in the nearshore/onshore areas can become floating debris.” This event also highlighted the consequences of large debris elements such as shipping containers, boats, barges, and unrestrained storage containers (Robertson et al. 2007).

Following entrainment of debris elements within the inundating flow, debris transport is affected by both the debris itself and the environment through which it moves (Stolle et al. 2020; Park et al. 2021). Debris size, density, and buoyancy have the potential to affect transportation behavior during inundation, while land gradient, built environment density, and inundation depth and velocity affect the likelihood and consequences of debris interaction with structures (Naito et al. 2013).

Debris-structure interaction diverges into impact and damming phenomena. Impact typically induces a short duration peak force as debris strikes the structure or member. Damming typically induces longer duration forces of a lower magnitude that have the potential to slowly

yield a structure or member and further accumulate debris. Large debris such as fishing vessels, vehicles, and shipping containers have been observed to cause failure of structural elements, including rigid frames and exterior columns, following both the Indian Ocean tsunami of 2004 and the Japanese tsunami of 2011 (Saatcioglu et al. 2005; Carden et al. 2015).

In response to these and other devastating tsunami events, tsunami-resilient structural design standards were adopted in 2016 in the form of ASCE/SEI 7-16: Minimum Design Loads and Associated Criteria for Buildings and Other Structures (ASCE/SEI 2016). Debris damming considerations in the current edition of these standards, ASCE 7-22 (ASCE/SEI 2022), include two alternative methods of lateral load prediction based in-part on a minimum assumed closure ratio due to debris accumulation and an overall structure drag coefficient. These four components are evaluated herein as experimental results are compared to ASCE 7-22 predicted values.

Laboratory experiments regarding debris damming emerged in the field of hydraulic engineering under steady flow conditions representative of riverine flooding (Bocchiola et al. 2006; Schmocker and Hager 2011; Oudenbroek et al. 2018; Mauti et al. 2020). As of late, unsteady, transient flow conditions in recent laboratory experiments have attempted to better represent coastal inundation events (Stolle et al. 2018; Wütrich et al. 2019; Shekhar et al. 2020). While these studies signal a shift towards tsunami-specific debris damming experiments, most utilized small-scale debris and a limited flume width, which are factors that the experiment presented here aims to rectify.

Many of these experimental studies note a “surface swell” or unbalanced hydrostatic condition upstream and downstream of a flow obstruction. This presence of a free surface implies that assumptions for quadratic drag – namely a fully-submerged flow obstruction in an infinite fluid field – deteriorate when applied to surface-piercing flow obstructions common in coastal inundation events. As a result, some recent tsunami literature (Stolle et al. 2018; Mauti et al. 2020) has adopted the use of a resistance coefficient (C_r) to capture both form drag and hydrostatic components of flow resistance by a fixed, surface-piercing obstacle. In this study, resistance coefficient is explored in contrast to ASCE 7-22 empirical drag coefficients for rectilinear structures.

While extensive research has been performed to understand tsunami debris impact forces, tsunami debris damming remains in need of further research (Nistor et al. 2017). The highly-varied, transient nature of tsunami overland flow and the stochastic nature of debris entrainment,

transport, and deposition against a coastal structure calls for a more thorough understanding of these processes. A thorough examination of current tsunami debris damming load predictions (ASCE/SEI 2022) has yet to be performed. As such, this study aims to:

- assess conservatism of ASCE 7-22 Equations 6.10-1 (Eq. 2) and 6.10-2 (Eq. 3) in quantifying lateral force-resisting system (LFRS) design loads under tsunami-induced debris damming;
- evaluate ASCE 7-22 Section 6.8.7 minimum closure ratios via a new photogrammetric method to estimate the submerged projected area of ephemeral debris dams under unsteady, transient flow conditions; and
- improve ASCE 7-22 Table 6.10-1 drag coefficients for rectilinear structures by exploring the application of bulk resistance coefficients to the column arrays of elevated coastal structures.

2.4 Background

2.4.1 Debris Damming Experiments

Many previous debris damming experiments (Bocchiola et al. 2006; Schmocker and Hager 2011; Oudenbroek et al. 2018) investigated large woody debris (LWD) damming in the presence of bridge decks and piers under simulated riverine conditions. Other steady-flow experiments employed idealized dam shapes and porosities rather than naturally-accumulating LWD elements (Mauti et al. 2020). More exploration must be conducted to examine the application of riverine debris damming findings to tsunami-resilient engineering design (Nistor et al. 2017), specifically with respect to the greater diversity of tsunami-driven debris and the variable structure density of tsunami inundation zones.

A recent shift from steady to unsteady, transient flow has aimed to better represent the conditions surrounding coastal inundation events. Stolle et al. (2018) used a dam-break wave to assess debris damming forces of scaled shipping containers, LWD, and construction materials under supercritical flow conditions. Wütrich et al. (2019) used a vertical-release technique to generate a dry-bed surge in order to quantify LWD and shipping container debris damming forces against a structure of varying porosity. Shekhar et al. (2020) employed an unbroken wave - generated via error function paddle displacement resulting in a single long wave (Bridges et al. 2011) - to investigate impact and damming forces of multiple debris elements against a structure.

These studies provide a strong basis for bridging the gap from hydraulic to coastal engineering applications, but often used small-scale debris elements and a limited flume width. A number of these experiments, under both steady (Schmocker and Hager 2011; Mauti et al. 2020) and unsteady flows (Stolle et al. 2018), discussed free-surface elevation increases upstream of a flow obstruction described as a "surface swell," resulting in unbalanced hydrostatic forces.

2.4.2 Resistance Coefficient of Surface-Piercing Flow Obstructions

While ASCE 7-22 provides overall drag coefficients for rectilinear structures, a bulk resistance coefficient commonly seen in hydraulic engineering may be a more suitable measure of flow resistance by an array of surface-piercing obstacles. Drag coefficient traditionally pertains to fully-submerged flow obstructions and is used to calculate force on the obstacle due to form drag only. Previous open channel experiments have explored the use of a modified drag coefficient, commonly termed a resistance coefficient, in attempts to capture the more complex hydrodynamics surrounding a surface-piercing flow obstruction.

Chaplin and Teigen (2003) found that loads on a surface-piercing cylinder towed at a steady velocity through a basin of quiescent water were due to both "flow separation and wavemaking," or a form drag component and a free-surface disturbance component. Fenton (2003) and Qi et al. (2014) each explored methods of predicting free-surface increases upstream of a flow obstruction by equating the drag force acting on the obstacle to the change in momentum flux upstream and downstream of the obstacle. While Fenton focused mainly on subcritical flows and noted that some assumptions degraded as flows became transitional, Qi et al. examined mainly choked, supercritical flows that generated hydraulic jumps downstream of the flow obstruction. Both studies retained the use of drag coefficient throughout their derivations which differs from more recent studies, described below.

Recent tsunami-related literature has shown a departure from drag coefficients of surface-piercing obstacles, instead opting to use resistance coefficient as a dimensionless measure of flow resistance. Arnason et al. (2009) described the use of resistance coefficient in transient flow experiments as a method to incorporate free-surface effects due to unbalanced hydrostatic pressure components. Stolle et al. (2018) echoed this, describing resistance coefficient as "a surrogate representing the force from both the form drag and the hydrostatic pressure." Mauti et al. (2020) once again referenced this hydrostatic imbalance, explicitly describing "the change in

water depth directly in front of and behind the column." Such descriptions reinforce the earlier observations of Chaplin and Teigen (2003) that flow separation and wavemaking components are not readily separable in hydrodynamic forces. This combination leads to a total resistance force described by a dimensionless resistance coefficient, analogous to a drag force described by a dimensionless drag coefficient.

The use of "bulk" in describing a bulk resistance coefficient is intended to account for interactions between individual columns as they contribute to a resistance coefficient for the entire column array. Rather than quantify blockage (local flow acceleration between flow-perpendicular obstructions) and sheltering (local flow deceleration due to upstream flow obstructions) for each individual column, bulk resistance coefficient captures the net result of all such interferences into a single dimensionless resistance coefficient (Gijón Mancheño et al. 2021).

2.4.3 Adoption of Tsunami-Resilient Design Standards

Spurred by consequential events including the: Indian Ocean earthquake and tsunami (2004), Samoan earthquake and tsunami (2009), Chilean earthquake and tsunami (2010), Tohoku tsunami (2011), and Sulawesi earthquake and tsunami (2018), a number of design guidelines were proposed for vertical evacuation refuge structures (VERS) which included considerations for debris damming. An early version of this was FEMA P-646 (FEMA 2012) which accounted for "damming of accumulated waterborne debris" in Section 6.5.7. The proposed equation (Eq. 1) took a similar form to the quadratic drag law and is based on maximum momentum flux (hu^2), fluid mass density including entrained sediment (ρ_s), width of debris dam taken as the length of a standard 6.10 m (20 ft) shipping container at minimum (B_d), and an empirical drag coefficient (C_d) of 2.0. The resulting horizontal debris damming force, F_{dm} , was to be applied as a uniformly distributed load over the extents of the debris dam. Further input definitions can be found in FEMA 2012.

$$F_{dm} = \frac{1}{2}\rho_s C_d B_d (hu^2)_{max} \quad (1)$$

ASCE/SEI 7-16: Minimum Design Loads and Associated Criteria for Buildings and Other Structures included "the first national, consensus-based standard for tsunami resilience" (ASCE/SEI 2016; Chock 2016). Tsunami resilience, defined as "the ability to prepare and plan

for, absorb, recover from, and more successfully adapt to adverse events" (NAS 2012), is particularly applicable to the design of VERS as well as critical and essential facilities. The current edition of these standards (ASCE/SEI 2022) includes the following tsunami loading considerations: hydrostatic, hydrodynamic, buoyancy and uplift, debris impact and damming, and foundation design parameters.

A host of experiments regarding debris impacts, particularly shipping containers and LWD, were performed in the years surrounding tsunami design adoption in 2016. Aghl et al. (2014) investigated axial impacts of shipping containers in a combined numerical and physical modelling campaign. Ko et al. (2015) investigated shipping container impacts in both air and water, employing the same error function wave generation method used in the experiment herein, as well as Bridges (2011) and Shekhar et al (2020). Ikeno et al. (2016) performed a similar physical experiment to assess the impact force of LWD at various angles of approach. While debris impact has been rigorously studied surrounding implementation of tsunami design into ASCE 7 standards, debris damming considerations have not been as thoroughly evaluated through physical model studies.

Regarding the comparison of experimental results to current tsunami-resilient design standards, pertinent sections of ASCE 7-22 (ASCE/SEI 2022) have been identified and presented here. ASCE 7-22 Section 6.2 defines the closure ratio of a structure as the: "ratio of the area of enclosure, not including glazing and openings, that is inundated to the total projected vertical plane area of the inundated enclosure surface exposed to flow pressure." From this measure, this section defines open structures as: "A structure in which the portion within the inundation depth has no greater than 20% closure ratio, and in which the closure does not include any Tsunami Breakaway Walls, and which does not have interior partitions or contents that are prevented from passing through and exiting the structure as unimpeded waterborne debris." Conversely, those structures that exceed 20% closure ratio are considered closed structures. From these classifications of open versus closed structures, minimum closure ratios for load determination are assigned in ASCE 7-22 Section 6.8.7: "… loads on buildings shall be calculated assuming a minimum closure ratio of 70% of the inundated projected area along the perimeter of the structure, unless it is an Open Structure as defined in Section 6.2. The load effect of debris accumulation against or within the Open Structure shall be considered by using a minimum closure ratio of 50% of the Inundated Projected Area along the perimeter of the Open Structure."

Regarding incident flow considerations, the ASCE 7-22 equation for detailed hydrodynamic lateral forces references Tsunami Inundation Load Case 2, defined as "…depth at two-thirds of maximum inundation depth when the maximum velocity and maximum specific momentum flux shall be assumed to occur in either incoming or receding directions."

ASCE 7-22 identifies two alternative methods for overall lateral force-resisting system design loads. The first method, a simplified equivalent uniform lateral static pressure (ASCE 7-22 Eq. 6.10-1, Eq. 2) applies an equivalent maximum uniform pressure, ρ_{uw}, to account for unbalanced lateral hydrostatic and hydrodynamic loads.

$$\rho_{uw} = 1.25 I_{tsu} \gamma_s h_{max} \tag{2}$$

where ρ_{uw} = equivalent maximum uniform pressure, applied over 1.3 times h_{max} ; I_{tsu} = tsunami importance factor; γ_s = minimum fluid weight density for design hydrostatic loads; h_{max} = maximum inundation depth above grade plane at the structure.

The alternative method, detailed hydrodynamic lateral forces (ASCE 7-22 Eq. 6.10-2, Eq. 3), includes additional building and incident flow characteristics.

$$F_{dx} = \frac{1}{2} \rho_s I_{tsu} C_d C_{cx} B (h_{sx} u^2) \tag{3}$$

where F_{dx} = drag force on the building or structure at each level; ρ_s = minimum fluid mass density for design hydrodynamic loads; I_{tsu} = tsunami importance factor; C_d = drag coefficient for the building as given in ASCE 7-22 Table 6.10-1; C_{cx} = proportion of closure coefficient; B = overall building width; h_{sx} = story height of story x; u = tsunami design flow velocity.

This method references a proportion of closure coefficient, C_{cx} (ASCE 7-22 Eq. 6.10-3, Eq. 4), taken as no less than the minimum closure ratio for load determination described above.

$$C_{cx} = \frac{\sum (A_{col} + A_{wall}) + 1.5 A_{beam}}{B h_{sx}} \tag{4}$$

where C_{cx} = proportion of closure coefficient, taken as no less than the closure ratio given in Section 6.8.7; A_{col}, A_{wall} = vertical projected area of all individual column and wall elements, respectively; A_{beam} = combined vertical projected area of the slab edge and the deepest beam exposed to the flow; B = overall building width; h_{sx} = story height of story *x.*

This method also references an empirical drag coefficient, C_d, of the structure based on building width to inundation depth ratio, B/h, given by ASCE 7-22 Table 6.10-1. For B/h ratios less than or equal to 12, a C_d of 1.25 is used, which is representative of all tested conditions in

this study. For B/h ratios equal to 60, a C_d of 1.75 is used and for B/h ratios greater than or equal to 120, a C_d of 2.0 is used. This table allows for interpolation as well.

2.5 Experimental Setup

2.5.1 Wave Flume and Incident Wave Conditions

This experiment was performed in the Large Wave Flume (LWF) of the O.H. Hinsdale Wave Research Laboratory (HWRL) at Oregon State University (Figure 2.1 and 2.2). The LWF was 104 m long, 3.7 m wide, and 4.6 m deep with an adjustable bathymetry comprised of 3.7 m square reinforced concrete panels. The LWF was equipped with a piston-type wavemaker capable of a 4 m maximum stroke and a 4 m/s maximum stroke velocity.

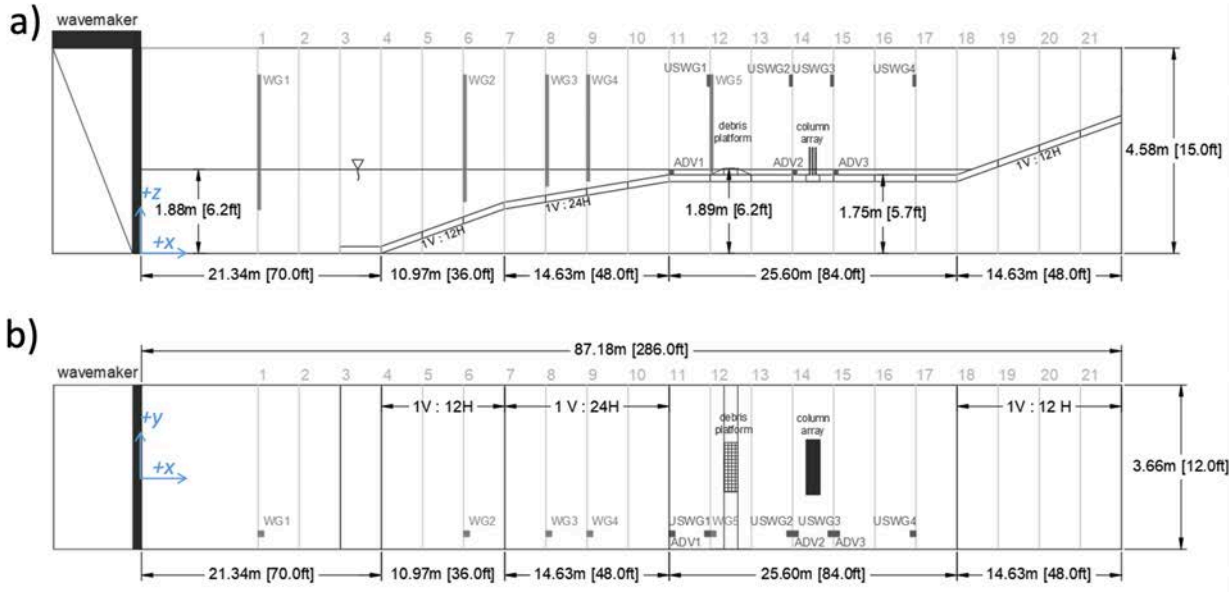

Fig 2.1. LWF experimental setup at HWRL (not to scale, pertinent extents shown); (a) elevation, (b) plan view; ADV = acoustic doppler velocimeter, WG = resistance wave gauge, USWG = ultrasonic wave gauge.

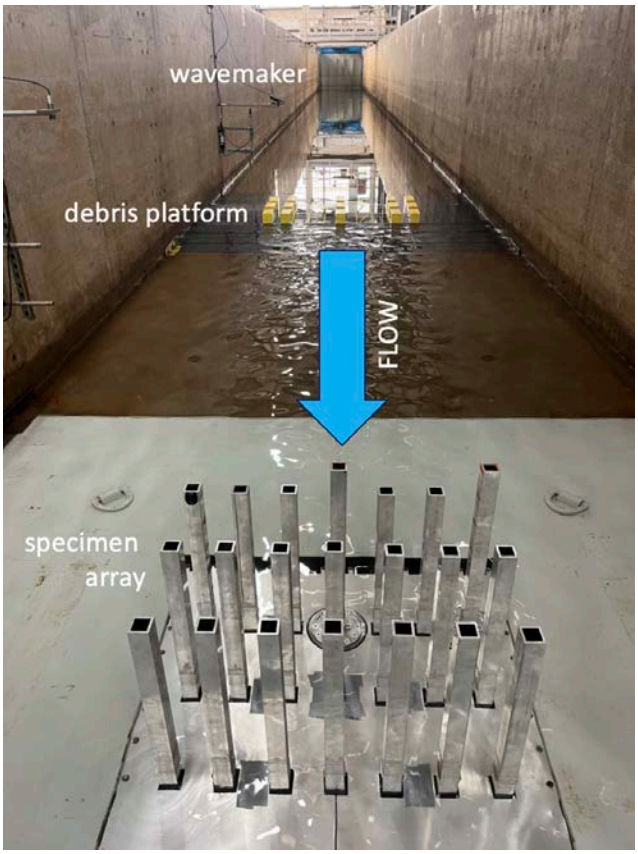

Fig 2.2. Annotated photo of LWF experimental setup, relative positions shown.

The bathymetric profile induced depth-limited breaking of incident waves, resulting in a broken tsunami-like bore propagating over a wet bed throughout the level test section. The bore-front turbulence and observed flow modification over the debris platform aimed to model tsunami overland flow landward of a large debris source, such as a port container facility. The coordinate space used in the LWF was as follows: + x in the direction of wave propagation (north) with $x = 0$ m at the neutral position of the wavemaker; + z in the vertical up direction with $z = 0$ m at the LWF floor; + y to the left (west) when facing the direction of wave propagation with $y = 0$ m at the centerline of the LWF.

Incident waves were generated by error function (ERF) wavemaker displacement at various scale factors (Bridges et al. 2011). Rather than conventional solitary wave generation techniques, ERF wave generation maximizes the inundation duration even for relatively small wave amplitudes by using the full 4 m wavemaker stroke. By rescaling the error function curve with the y-axis scaled to wavemaker displacement and the x-axis scaled to time of displacement

(Figure 2.3), three incident wave conditions were selected for this experiment (Table 2.1, Figure 2.4). These three ERF scales were selected by visual observation then confirmed via Froude similitude to field studies of tsunami flow in the presence of structures (Fritz et al. 2012; Matsutomi et al. 2010), with estimated Froude regimes between 0.4 and 2.0. While this wave generation method represents an improvement relative to solitary wave generation, the experimental inundation period and volume of water displaced is still much lower than a realistic tsunami. This has implications regarding the experimental debris dams in this study, potentially limiting debris accumulation and subsequent damming loads observed at laboratory scale. Incident waves are referred to as Wave A, Wave B, and Wave C herein and ERF 300, ERF 400, ERF 500 in external data structures, respectively.

Table 2.1. Error function-generated incident wave hydrodynamic conditions at midpoint of column array; midpoint of column array interpolated via ADV2/ADV3, USWG2/USWG3.

Incident wave	U_{max} *(m/s)*	η_{max} *(m)*
Wave A	1.59	0.40
Wave B	1.27	0.35
Wave C	1.14	0.32

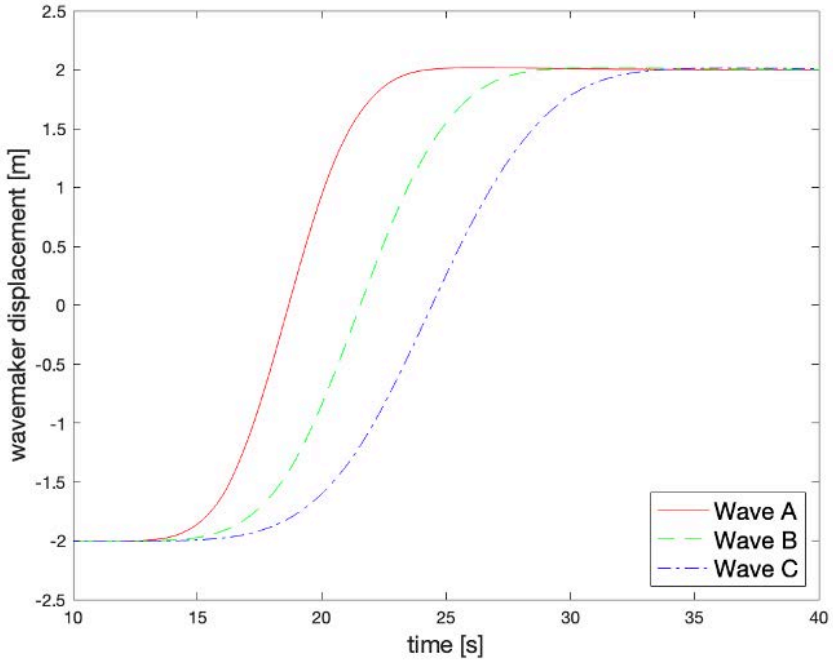

Fig 2.3. Wavemaker displacement during ERF wave generation.

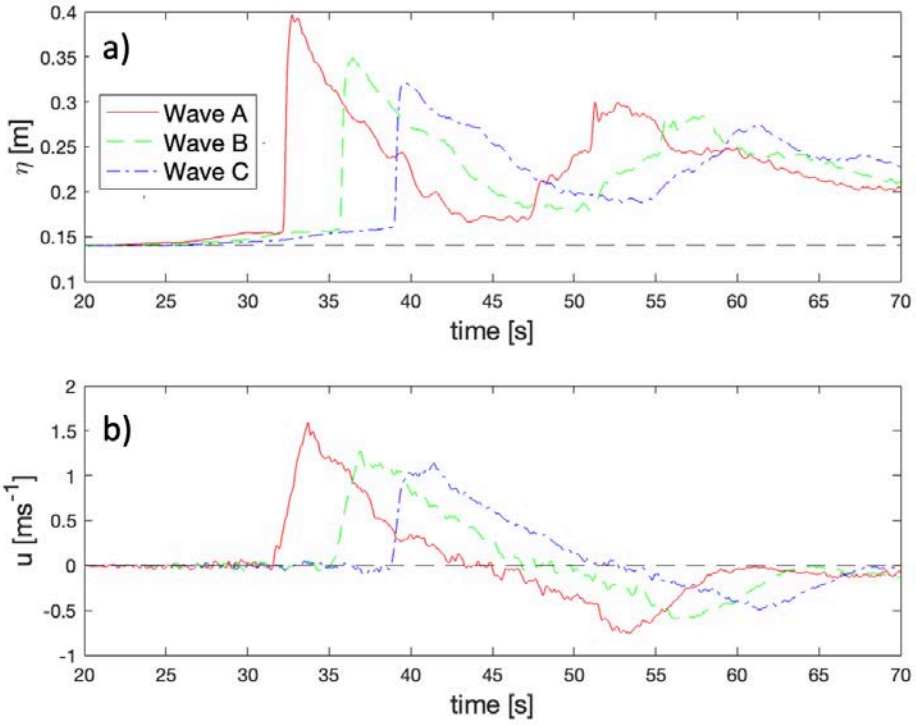

Fig 2.4. Mid-specimen (a) free surface displacement relative to flat test section elevation and (b) flow velocity; midpoint of column array interpolated via ADV2/ADV3, USWG2/USWG3.

2.5.2 Column Specimen and Debris Elements

The experimental specimen consisted of a column array representing a pile group supporting an elevated coastal structure. The column array was underlain by a six-degree of freedom force balance plate. The column array allowed for interchangeable column configurations of 3 rows with 3, 5, or 7 columns per row (Table 2.2, Figure 2.5). By varying configuration of the column array, both open and closed structure classifications from ASCE 7-22 Section 6.8.7 were considered in this physical model. Experimental ratios of column width *(b)* to flow-perpendicular column spacing *(d)* may not be representative of prototype-scale structures, see Discussion for further commentary on specimen scaling.

Table 2.2. Experimental column array configurations, showing dimensions from Figure 2.5.

Column configuration	Closure ratio *(%)*	ASCE 7-22 Classification	*a* *(cm)*	*b* *(cm)*	*c* *(cm)*	*d* *(cm)*	*e* *(cm)*	*f* *(cm)*
3x3	15.8	Open	122	5.1	12.2	39.7	30.0	21.9
3x5	26.3	Closed	122	5.1	12.2	16.8	30.0	21.9
3x7	36.8	Closed	122	5.1	12.2	9.2	30.0	21.9

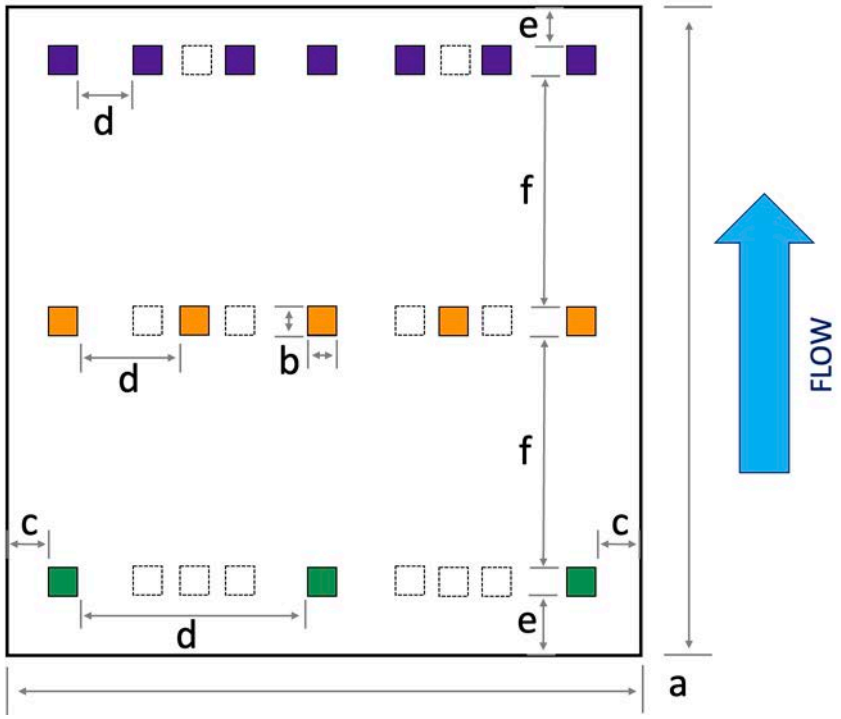

Fig 2.5. Schematic of column array specimen dimensions (see Table 2.2);
3x3 configuration = green, 3x5 configuration = orange; 3x7 configuration = purple.

Debris elements discussed in this study include 1:20 geometric scale standard 6.1 m (20 ft) and 12.2 m (40 ft) shipping containers (SC) (6.1 m SC: 0.30 m L x 0.11 m W x 0.11 m H; 12.2 m SC: 0.60 m L x 0.11 m W x 0.11 m H). The debris elements were constructed of laminated Douglas fir lumber, then sealed and painted with orienting markings. Debris element dimensions were scaled, however masses (6.1 m SC: 2.17 kg; 12.2 m SC: 4.21 kg) were not, resulting in higher masses at prototype scale (6.1 m SC: 17,400 kg; 12.2 m SC: 33,700 kg) than fully-loaded shipping containers – provided by ASCE 7-22 Table 6.11-2: Weight and Stiffness of Shipping Container Waterborne Floating Debris – by a factor of 1.3 and 2.0 for 6.1 m and 12.2 m shipping containers, respectively. Debris element masses were regularly recorded throughout testing to ensure no change in mass due to water absorption.

2.5.3 Instrumentation

Free-surface elevation was measured via five surface-piercing resistance wave gauges (WG, Dibble and Sollitt 1989) and four ultrasonic wave gauges (USWG, TS-30S1-IV, Senix, Hinesburg, Vermont). Flow velocity was recorded via three acoustic doppler velocimeters (ADV, Nortek Vectrino+, Nortek, Rud, Norway) which were included in hydrodynamic trials

lacking debris, but were removed prior to debris trials to avoid debris elements striking the submerged instruments. Sensor names, consistent with Figure 2.1, and locations relative to the LWF coordinate space are provided in Table 2.3.

Table 2.3. Hydrodynamic instrumentation layout relative to LWF coordinate space.

Sensor name	*X* *(m)*	*Y* *(m)*	*Z* *(m)*
WG1	10.30	-1.39	--
WG2	28.59	-1.38	--
WG3	35.89	-1.38	--
WG4	39.55	-1.37	--
WG5	50.48	-1.46	--
USWG1	50.51	-0.93	3.03
USWG2	57.79	-1.37	3.33
USWG3	61.44	-1.36	3.33
USWG4	68.76	-1.37	3.33
ADV1	50.49	-1.29	1.77
ADV2	57.79	-1.64	1.77
ADV3	61.42	-1.65	1.77

The full column array was underlain by a six-degree of freedom force balance plate (FBP, AF 32-12-K, Advanced Mechanical Technology Inc (AMTI), Watertown, MA) to measure total forces and moments acting on the array. An additional six-degree of freedom pancake load cell (LC, Omega191 SI 7200-1400, ATI, Apex, North Carolina) was installed atop the FBP to record forces and moments acting on the center column of the seaward row individually.

Plan view recordings of the full experimental extents- debris platform through column specimen- were captured via four down-facing 4K HD CCTV cameras (RLC-810A, Reolink, New Castle, Delaware) with overlapping fields of view. An isometric view of the column array was captured via another camera (HERO11 Black, GoPro, San Mateo, California) mounted on the LWF wall above the still water level.

2.6 Methods

2.6.1 Experimental Procedure

Prior to column array installation, preliminary trials were performed to identify the debris orientation that maximized the number of debris elements passing through the column array footprint. During later debris trials, the quantity and orientation of debris was kept consistent for each debris type, shown in Figure 2.6.

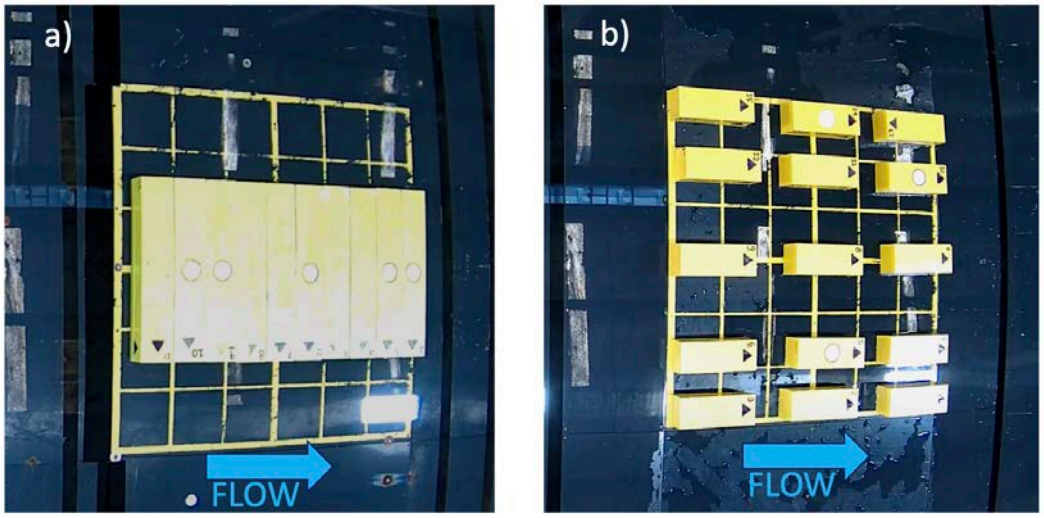

Fig 2.6. Initial debris element configuration on debris platform and inundation flow direction for (a) 12.2 m shipping container and (b) 6.1 m shipping container debris elements.

For each experimental trial (Figure 2.7), the data acquisition system (DAQ) was started, triggering the force balance plate (FBP) and hydrodynamic instruments, while cameras were started manually. Video recordings were later synchronized with the corresponding data by referencing bore arrival at the seaward row of columns. DAQ and FBP time-series were recorded for 200 seconds, the DAQ sampling at 100Hz and the FBP sampling at 1000Hz. Video recordings were stopped manually upon completion of return flow, upon which the research team would enter the flume to reset debris for the succeeding trial. Following the resetting of debris, the flume was left undisturbed as free-surface variations settled out, resulting in approximately 20 minutes elapsed between successive trials.

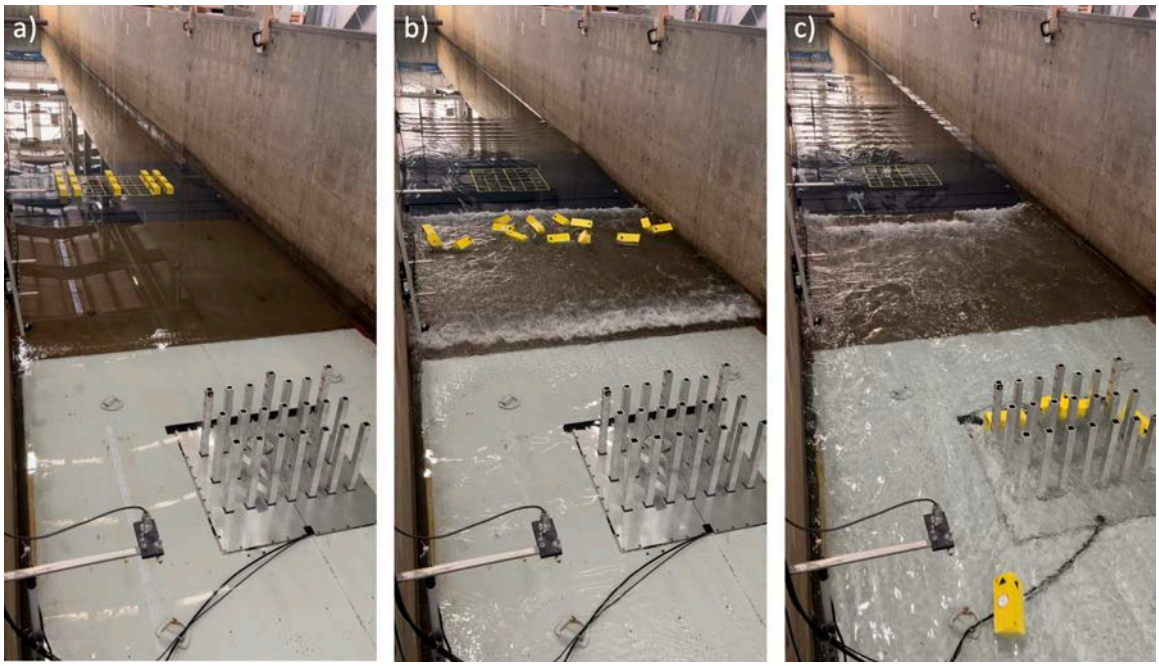

Fig 2.7. Example experimental trial (Wave C, 6.1 m SC, 3x7 column array) showing phases of a) pre-bore arrival, b) debris transport, and c) debris damming against structure.

2.6.2 Photogrammetry Analysis

A method for photogrammetric analysis of in-situ debris dams was developed and validated to estimate submerged projected areas of experimental debris dams. Debris dams were then analyzed using this method at times of horizontal force local maxima during both debris accumulation and quasi-steady phases of debris damming (Figure 2.8). Debris dams were classified as either debris accumulation phase while debris were still actively aggregating against the column array or as quasi-steady phase when the debris dam was no longer subject to further debris accumulation or reshuffling under the inundation flow. Raw FBP horizontal force data was low-pass filtered to isolate the debris damming signal (after Shekhar et al. 2020) with frequencies above 5 Hz omitted, frequencies below 2.5 Hz retained, and a weighted transition zone between 2.5 and 5 Hz, as shown in Figure 2.8.

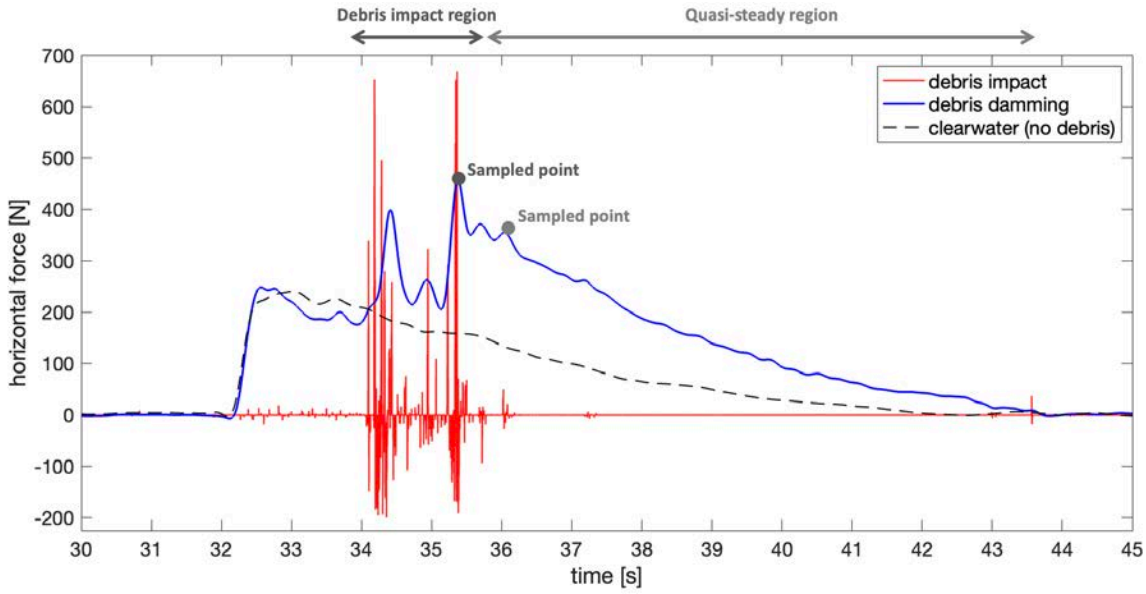

Fig 2.8. Example FBP time-series, showing omitted debris impact signal (red), retained debris damming signal isolated via weighted low-pass filtering (blue), and low-pass filtered clearwater force (black dashed line) for comparison.

At each timestamp of photogrammetric analysis, the following method was performed: First, damming angle of each element relative to the incident flow was estimated at 15 degree intervals and a raw projected area was calculated via trigonometric projection of a rectangular prism. Next, the proportion of each element exposed to incident flow was estimated as a percent area by visual inspection of synchronized video perspectives, correcting for shielding and overlapping of debris and resulting in a corrected projected area. Similarly, next, the submerged proportion of each element was estimated, again by visual estimation of percent area, correcting for incomplete submersion and resulting in a submerged projected area. Finally, the submerged projected area of any columns not shielded by debris was calculated and summed along with the element-wise submerged projected areas of all debris elements.

This photogrammetric method was validated using 26 dam test cases, in which debris type, quantity, position, damming angle, and water depth were varied to replicate debris dams similar to those observed in the experiment. For each dam test case, the following method was performed (Figure 2.9): Video was recorded circumscribing the column array, including the test case debris elements and a 1 m reference square (Fig 2.9a), then converted to a three-dimensional point cloud (Fig 2.9b). Next, the three-dimensional point cloud was rectified into a flow-aligned orthographic projection (Fig 2.9c). The flow-aligned orthographic projection was

imported into a CAD program (AutoCAD 2022, Autodesk) and re-scaled based upon the 1 m reference square (Fig 2.9d). Finally, projected area of the test case was outlined and measured, with an approximate 5% error based on known dimensions of the column specimen.

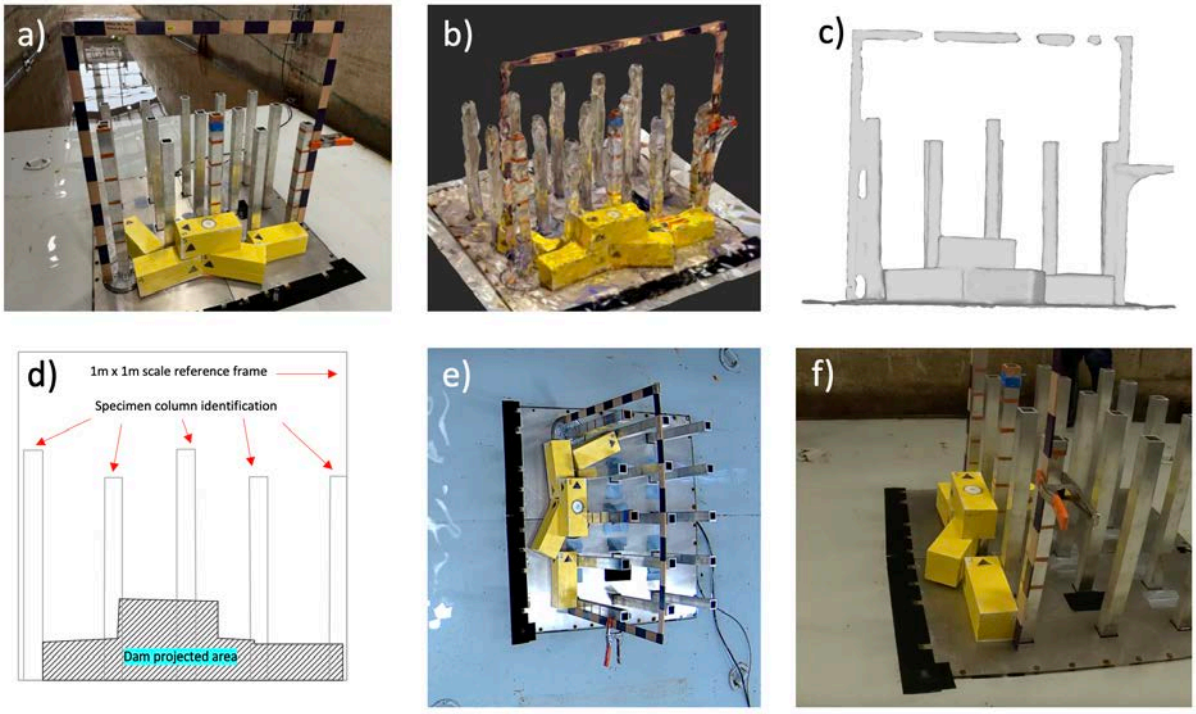

Fig 2.9. Debris dam test case projected area calculation for photogrammetry method validation; (a) example test case; (b) three-dimensional .obj file of scanned test case; (c) flow-aligned orthographic projection of scanned test case; (d) measured projected area of test case, re-scaled in AutoCAD according to 1 m reference frame; (e) plan view and (f) isometric view of test case used during photogrammetry method analysis.

These measured areas of dam test cases were then compared to estimated areas obtained via the proposed photogrammetric method. The 26 test cases were subdivided as a means of validating specific attributes of the photogrammetric method: 10 cases estimating total projected area in 4 cm of water (total projected area, minimal confounding effects of submersion), 8 cases estimating total projected area in 13 cm of water (total projected area, increased effects of submersion), and 8 cases estimating submerged projected area in 13cm of water (full intended scope of photogrammetric method). Validation results are shown in Table 2.4 and Figure 2.10, resulting in 5% mean absolute percentage error (MAPE) in estimated submerged projected areas of experimental debris dams.

Table 2.4. Summary of photogrammetric method validation results.

Estimated value	SWL *(cm)*	RMSE *(m^2)*	MAPE *(%)*
total projected area, A_p	4.0	0.0081	6.9
total projected area, A_p	13.0	0.0020	2.9
submerged projected area, A_{sp}	13.0	0.0034	5.0

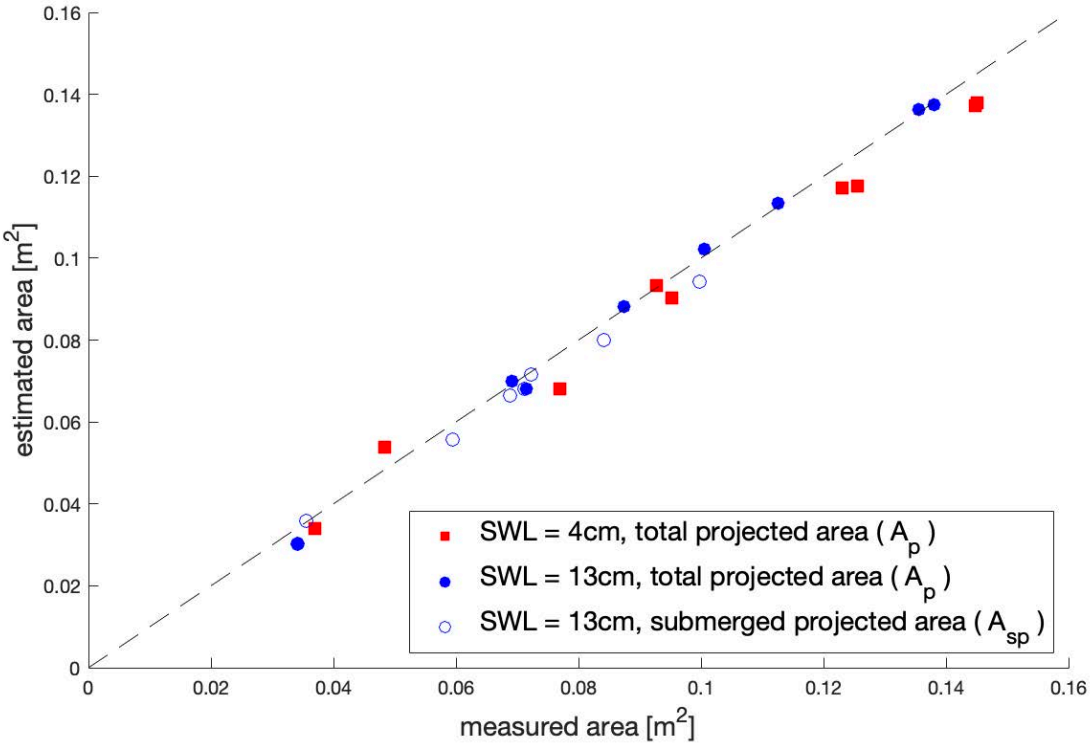

Fig 2.10. Results of photogrammetric method validation campaign.

2.7 Analysis

Figure 2.11 shows experimental horizontal forces at local maxima due to debris damming (as shown in Figure 2.8) in comparison to lateral-force-resisting system (LFRS) design loads per ASCE 7-22 Section 6.10 (ASCE/SEI 2022). The dashed (3x3, 3x5) and dash-dot lines (3x7) represent the simplified equivalent uniform lateral static pressure of ASCE 7-22 Equation 6.10-1 (Eq. 2) calculated for each wave condition applied as a uniform pressure over the submerged projected area of the column array to 1.3 times the calculated maximum inundation depth. Because the column array was intended to model a VERS or critical facility, a tsunami

importance factor of 1.25 is applied throughout. The solid line shows the detailed hydrodynamic lateral forces predicted by ASCE 7-22 Section 6.10.2. The tested 3x3 configuration is classified as an open structure per ASCE 7-22, while the tested 3x5 and 3x7 configurations are classified as closed structures, hence the combined figure panels and identical detailed hydrodynamic lateral design loads. Here, horizontal forces are plotted against inundation Froude number, calculated as:

$$Fr = \frac{u}{\sqrt{g(\eta)}} = \frac{u}{\sqrt{g(H+h)}} \tag{2}$$

where Fr = instantaneous inundation Froude number; u = instantaneous inundation flow velocity; g = gravitational acceleration; η = instantaneous free surface elevation above flume bathymetry; H = instantaneous bore height above still water level (SWL); h = still water level (SWL).

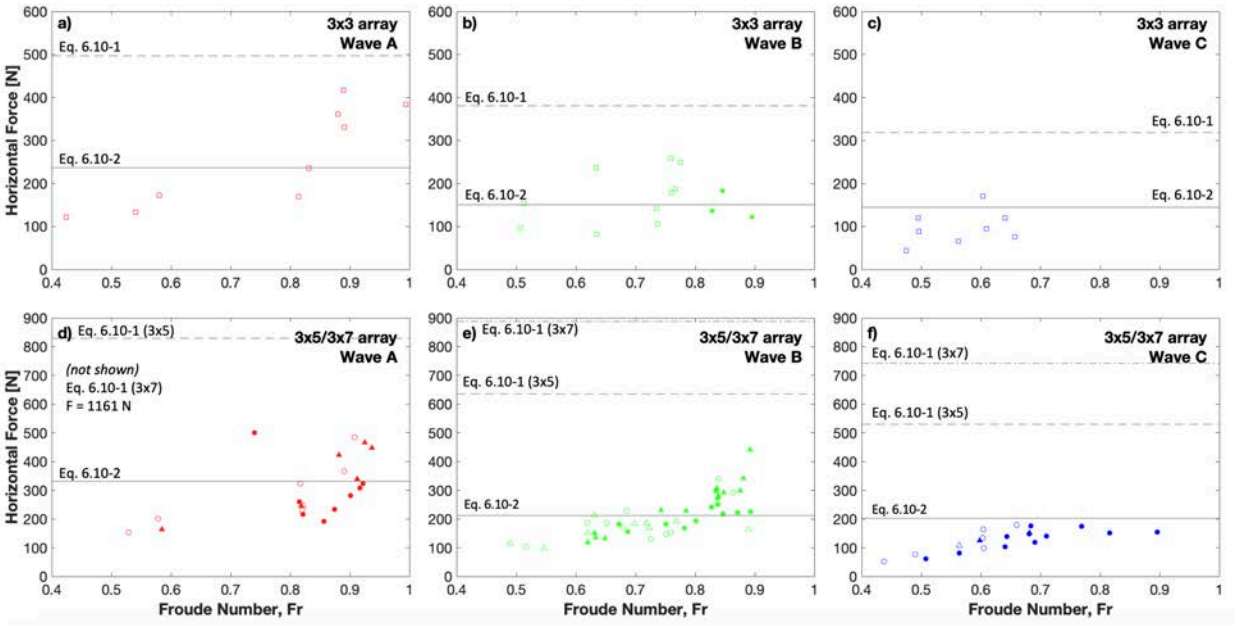

Fig 2.11. Comparison of experimental debris damming forces to ASCE 7-22 Section 6.10 Equations 6.10-1 and 6.10-2 (Eq. 2 and 3, respectively) for lateral-force-resisting system design loads; red = Wave A; green = Wave B; blue = Wave C; square = 3x3; circle = 3x5; triangle = 3x7; filled symbol = 6.1 m SC; open symbol = 12.2 m SC.

Figure 2.11 shows that relative to the experimental debris damming forces, ASCE 7-22 Equation 6.10-1 (Eq. 2) is conservative in all experimental cases. For the most energetic incident wave, Wave A, the mean factor of safety (FS, the ratio of design capacity (ASCE 7-22 design load) to applied (experimental) forces) for 12.2 m shipping containers damming against a 3x3

column configuration is 1.9 and could be considered reasonable for design. For the same wave condition and debris type, mean FS increases to 2.8 and 4.7 for 3x5 and 3x7 column configurations, respectively. Under the same conditions, 6.1 m shipping containers exhibit slightly lower mean FS of 2.7 and 3.3 for 3x5 and 3x7 column configurations, respectively. It should be noted that 6.1 m shipping containers were not regularly tested for the 3x3 column configuration because the longest diagonal dimension of the debris was less than the clear spacing of adjacent columns, limiting the potential for and likelihood of debris dam formation.

Under less energetic wave conditions, Wave B and C, mean FS generally increases, ranging from 2.3 (Wave B, 3x3, 12.2 m SC) to 6.9 (Wave C, 3x7, 12.2 m SC). This increase is due in part to the equivalent maximum uniform pressure being applied over the projected area of the structure, which increases by 1.7 and 2.3 for 3x5 and 3x7 column configurations, respectively, compared to the 3x3 column configuration projected area.

Contrary to the simplified equivalent uniform lateral static pressure method, ASCE 7-22 Equation 6.10-2 (Eq. 3) is often unconservative relative to the debris damming forces observed in this experiment. Generally, this equation is least conservative at higher inundation Froude regimes (Fr). The lowest Fr inundation condition, Wave C, shows only one example of unconservative load prediction (Wave C, 3x3, 12.2 m SC) among all experimental debris damming forces. At more energetic incident wave conditions, Wave A and B, ASCE 7-22 Equation 6.10-2 (Eq. 3) load prediction is often unconservative at higher instantaneous Fr numbers, exceeded by all three tested column configurations and both tested debris types.

In comparing mean factors of safety (FS), Wave C resulted in reasonable values for design ranging from 1.5 (Wave C, 3x7, 6.1 m SC) to 1.9 (Wave C, 3x7, 12.2 m SC). While factors of safety between 1.5 and 2 may be acceptable for many applications, this may still be low considering the consequences associated with structural failure of VERS. For Wave A and B, mean FS values range from 0.9 (Wave B, 3x7, 6.1 m SC) to 1.3 (Wave A, 3x7, 12.2 m SC). FS values only slightly exceeding 1 are rare in design applications and those less than 1 imply insufficient structural capacity relative to the experimental forces. While mean FS provides a reasonable method to assess ASCE 7-22 Equation 6.10-2 (Eq. 3) generally, it should be noted that the predicted load is often exceeded under Wave A and B inundation cases. Mean FS can exceed 1 for certain tested conditions, but half or more individual debris damming cases may exceed the predicted load, such as Wave B, 3x5 and 3x7, 6.1 m and 12.2 m SC. As mentioned,

ASCE 7-22 load prediction uses both an assumed minimum closure ratio and overall structure drag coefficient as inputs, which have also been compared to experimentally-derived values.

Figure 2.12 shows experimental closure ratios in comparison to ASCE 7-22 minimum closure ratios per Section 6.8.7. Estimated dam areas, calculated via the photogrammetry method, are divided by the inundated vertical plane area of the column array at the time of debris dam analysis to derive the experimental closure ratios shown. ASCE 7-22 minimum closure ratios per Section 6.8.7 are shown as solid horizontal lines.

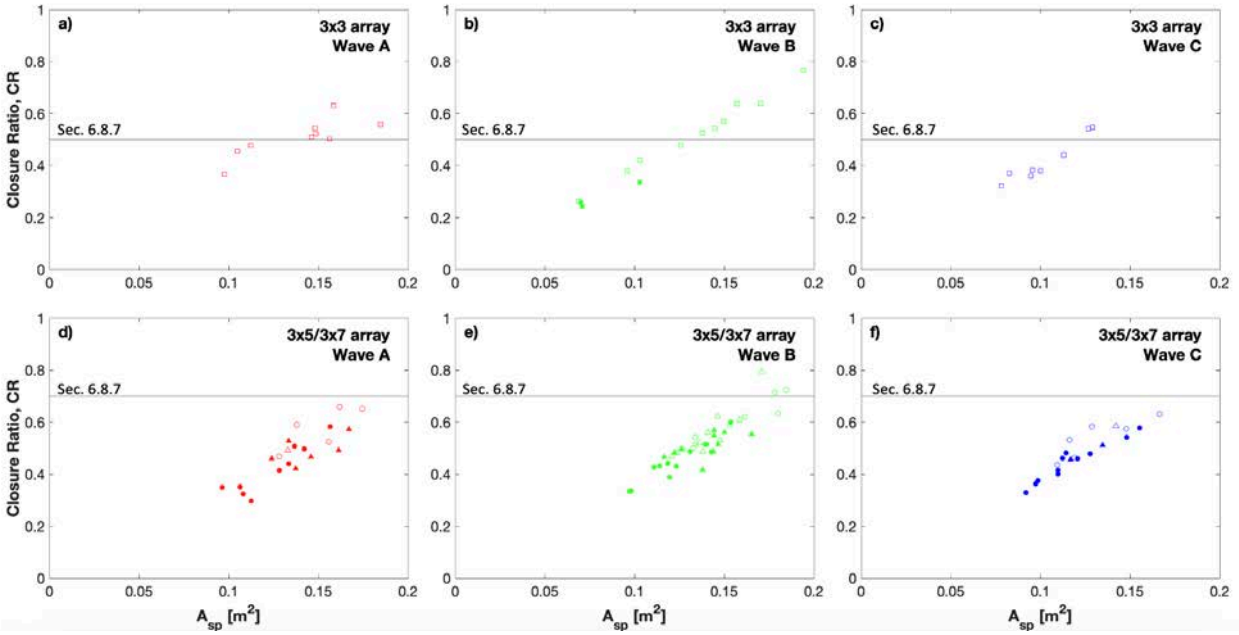

Fig 2.12. Comparison of experimental closure ratios to ASCE 7-22 Section 6.8.7 minimum closure ratios; red = Wave A; green = Wave B; blue = Wave C; square = 3x3; circle = 3x5; triangle = 3x7; filled symbol = 6.1 m SC; open symbol = 12.2 m SC.

Figure 2.12 shows that minimum closure ratios for load determination presented in ASCE 7-22 Section 6.8.7 are generally conservative for closed structures, but unconservative for open structures. The tested 3x3 column configuration represents an open structure (structure-only closure ratio less than 20%) while 3x5 and 3x7 configurations represented closed structures. The minimum closure ratio for closed structures of 70% was only exceeded by three experimental debris dams, all comprised of larger (12.2 m SC) debris elements. Conversely, the minimum closure ratio for open structures of 50% was exceeded by experimental debris dams under all three incident wave conditions. Particularly for Wave A and B, this minimum closure ratio is exceeded by half or more experimental debris dam cases.

Figure 2.13 shows bulk resistance coefficients of the tested column array configurations aggregated from all 3 incident wave conditions. These data were obtained by sampling hydrodynamic data (recorded and sampled at 100 Hz) and horizontal force data (recorded at 1000 Hz, downsampled at 100 Hz to match hydrodynamic data) over the inundation flow duration (when inundation flow velocity exceeds 10% of the maximum value) and calculating resistance coefficient via a modified quadratic drag equation (Mauti et al. 2020, Eq. 3). The vertical dashed line represents the drag coefficient of 1.25 proposed by ASCE 7-22 Table 6.10-1 based upon the width to inundation depth ratios of this experimental model.

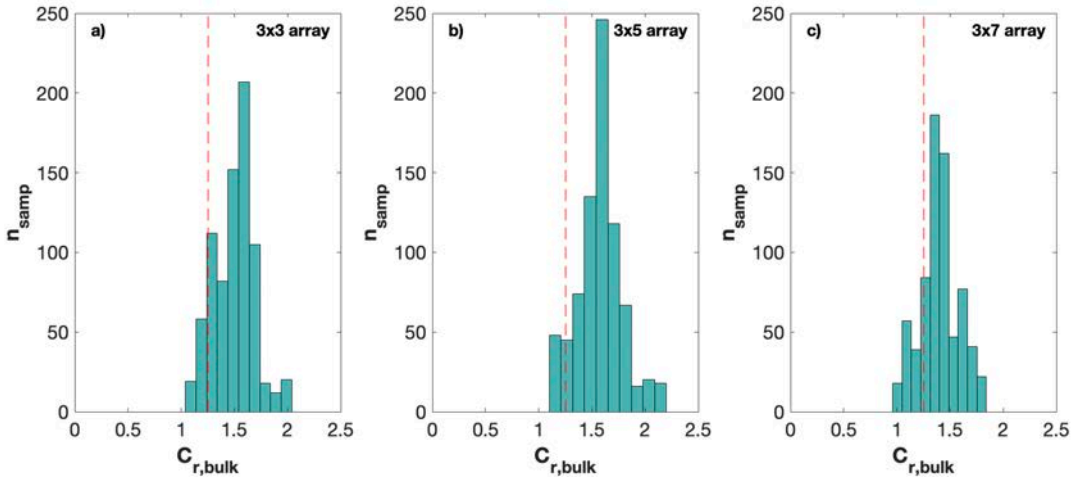

Fig 2.13. Comparison of experimental bulk resistance coefficients *($C_{r,\,bulk}$)* to ASCE 7-22 Table 6.10-1 drag coefficients for rectilinear structures; ASCE 7-22 Table 6.10-1 drag coefficient *(C_d)* shown by vertical red dashed line.

Table 2.5. Hydrodynamic bulk resistance coefficient statistics of each column configuration.

Column configuration	*ASCE 7-22* *(C_d)*	*Mean* *($C_{r,\,bulk}$)*	*Standard deviation* *($C_{r,\,bulk}$)*	*Median* *($C_{r,\,bulk}$)*
3x3	1.25	1.50	0.19	1.52
3x5	1.25	1.58	0.21	1.58
3x7	1.25	1.40	0.18	1.40

Figure 2.13 and Table 2.5 show that for all tested column configurations, experimental hydrodynamic bulk resistance coefficients *($C_{r,\,bulk}$)* regularly exceed the design drag coefficient given by ASCE 7-22 Table 6.10-1 for the building depth to inundation depth ratios of this

experiment. There is variability between mean $C_{r,\,bulk}$ values of the tested column configurations, likely due to variation in intercolumn effects of blockage and sheltering. Blockage is known to increase local flow velocity by channeling flow between flow-perpendicular obstructions while sheltering is known to decrease local flow velocity due to upstream obstructions shielding flow (Gijón Mancheño et al. 2021).

2.8 Discussion

While ASCE 7-22 Equation 6.10-1 (Eq. 2) is conservative for all debris damming forces observed in this experiment, it is often overconservative and may be impractical for design. Factors of safety (FS) exceeding 2.5 or 3 are rare in design, yet mean FS observed in this experiment often exceed 4 and reach as high as 6.9. This equation is sensitive to maximum inundation depth, h_{max}, which is used both in calculating the equivalent maximum uniform pressure and the height that this pressure is applied over, 1.3 times h_{max}. In contrast, it should be noted that this equation does not account for maximum inundation velocity, nor reference the inundation load cases of ASCE 7-22 Section 6.8.3.1. While ASCE 7-22 Equation 6.10-1 (Eq. 2) represents a simplified method of accounting for unbalanced lateral hydrostatic and hydrodynamic loads, it may be impractically conservative, especially at lower energy inundation flows and denser column configurations.

Figure 2.11 shows that relative to the experimental debris damming forces herein, ASCE 7-22 Equation 6.10-2 (Eq. 3) is not nearly as conservative as Equation 6.10-1 (Eq. 2). A key difference between these load prediction equations is that the former includes more factors relating to flow and structure characteristics while the latter is a simplified method. ASCE 7-22 Equation 6.10-2 (Eq. 3) references Tsunami Load Case 2 from ASCE 7-22 Section 6.8.3.1 but only utilizes u_{max} as an input value. Rather than two-thirds of h_{max}, this equation uses the average story height of the structure, h_{sx}, as a length term. In this experiment, h_{sx} was taken as 0.225 m (4.5 m at 1:20 geometric scale) to represent as-built story heights of existing VERS in both the United States of America and Japan (FEMA 2019).

Figure 2.12 shows that the minimum assumed closure ratio for closed structures is generally conservative under all but the most extreme circumstances, indicative of multiple large debris elements damming simultaneously. Conversely, the minimum assumed closure ratio for open structures appears much less conservative, often exceeded by relatively small submerged

projected dam areas slightly exceeding 0.12 m^2. In cases of 12.2 m shipping containers, the full building width can be more than covered by 2 elements damming end-to-end, indicating high sensitivity of closure ratio to large debris elements. Additional work including varied building widths, additional debris element dimensions, and heterogeneous debris fields may help to clarify this relationship.

Figure 2.13 shows that the drag coefficients for rectilinear structures given by ASCE 7-22 Table 6.10-1 do not capture those experimentally determined under the tested column configurations. Since the original publication of this table in ASCE 7-16 (ASCE/SEI 2016), multiple tsunami-related publications have adopted the use of resistance coefficient rather than drag coefficient (Stolle et al. 2018, Mauti et al. 2020). This is particularly applicable to surface-piercing obstacles like partially-inundated structures and accounts for flow-column interactions that may not be captured in drag coefficients for rectilinear structures of the same exterior dimensions. The lack of design conservatism seen in ASCE 7-22 Equation 6.10-2 (Eq. 3) may be due to this underestimation of dimensionless flow resistance of column arrays.

Mean $C_{r,\,bulk}$ for the 3x7 column configuration is closest to the value given by ASCE 7-22 Table 6.10-1, likely due to increased sheltering effect reducing inundation flow velocity on the second and third rows of the column array. Mean $C_{r,\,bulk}$ for the 3x3 column configuration is slightly further from the value given by ASCE 7-22 Table 6.10-1. Such a sparse seaward row of columns likely limits the effects of sheltering, but in turn also limits blockage effects. In other words, seaward columns may have little sheltering effect on subsequent rows, but also may not drastically channelize flow and increase flow velocity on downstream columns. Mean $C_{r,\,bulk}$ for the 3x5 column configuration is greatest compared to the value given by ASCE 7-22 Table 6.10-1, again likely due to blockage and sheltering. Relative to the 3x3 column configuration, blockage effects and sheltering effects are both likely to increase. Due to the relatively large stream-wise spacing of the column array, the increase in blockage likely outweighs the increase in sheltering, leading to a higher mean value of $C_{r,\,bulk}$.

A major benefit of discussing flow resistance in terms of bulk resistance coefficient is that these sheltering, blockage, and unbalanced hydrostatic force effects are all captured in addition to the form drag contribution of the structure (Stolle et al. 2018). This represents an improvement over modelling a pile-elevated coastal structure as a solid rectilinear structure per ASCE 7-22 Table 6.10-1.

It should be noted that a number of assumptions were made in this physical model. At 1:20 geometric scaling, the 5.1 cm wide columns would be 1.02 m wide at prototype scale, likely too wide to accurately represent columns of VERS. Additionally, story height was taken as 0.225 m, or 4.5 m at prototype scale, to represent existing VERS. This assumption has direct implications through the h_{sx} term in ASCE 7-22 Equation 6.10-2 (Eq. 3).

Further, flows at such shallow depths are more sensitive to bottom friction, thus affecting roughness and viscosity in terms of Reynolds scaling. Such scaling effects may lead to differences in these results compared to other similar studies or ASCE 7-22 standards. Additionally, due to laboratory limitations on water displacement and inundation duration, the experimentally-generated debris dams may have not have developed representatively of real-world debris dams subject to longer inundation durations. Similarly, the volume and quantity of incident debris was limited, potentially misrepresenting the volume and density of real-world debris fields (Nistor et al. 2017).

Finally, due to the transient nature of tsunami inundation flow, projected areas of debris dams were quantified as best as possible via the photogrammetric method explained herein, yet these are still to be taken as estimates.

2.9 Conclusions

The findings presented here represent comparisons of experimental debris damming metrics to those predicted in ASCE 7-22 Chapter 6: Tsunami Loads and Effects (ASCE/SEI 2022). Based on the results of this physical model experiment of tsunami debris damming forces:

1. ASCE 7-22 Equation 6.10-1 (Eq. 2), simplified equivalent uniform lateral static pressure, is conservative across all tested experimental conditions, reasonable for design under high energy incident waves, but potentially overly-conservative under lower energy inundation;
2. ASCE 7-22 Equation 6.10-2 (Eq. 3), detailed hydrodynamic lateral forces, is often unconservative at higher Froude regime inundation and larger debris elements, and appears particularly sensitive to inundation velocity;
3. ASCE 7-22 Section 6.8.7 minimum closure ratios are conservative for closed structures but often unconservative for open structures, especially in the presence of larger debris elements;

4. ASCE 7-22 Table 6.10-1 drag coefficients for rectilinear structures are often exceeded by experimental hydrodynamic bulk resistance coefficients; and
5. Bulk resistance coefficient may represent an improved dimensionless measure of flow resistance than the drag coefficients currently used in ASCE 7-22 load predictions.

This study represents a preliminary comparison of laboratory-scale experimental data to ASCE 7-22 tsunami-resilient design standards. Additional trials and similar studies should yield an improved understanding of debris damming forces. More work is needed to continue this investigation, particularly with varying structure and debris characteristics, to further assess the findings presented here.

2.10 Data Availability Statement

Some or all data, models, or code that support the findings of this study are available from the corresponding author upon reasonable request.

2.11 Acknowledgements

Funding for this research was provided by the National Science Foundation (NSF) Division of Civil, Mechanical, and Manufacturing Innovation (CMMI) and Natural Hazards Engineering Research Infrastructure (NHERI) through Grants #2203131, #2203116 and #2037914. The authors would like to thank the HWRL and CEOAS Machine and Technical Development Facility staff for their assistance in experimental setup and testing.

2.12 References

Aghl PI, CJ Naito, HR Riggs (2015) "Estimation of demands resulting from inelastic axial impact of steel debris." Engineering Structures, 82, 11–21. https://doi.org/10.1016/j.engstruct.2014.10.021

Arnason H, C Petroff, H Yeh (2009) "Tsunami bore impingement onto a vertical column." Journal of Disaster Research, 4(6), 391–403. https://doi.org/10.20965/jdr.2009.p0391

ASCE/SEI (2016) "Minimum design loads for buildings and other structures." ASCE/SEI 7-16, Reston, VA.

ASCE/SEI (2022) "Minimum design loads for buildings and other structures." ASCE/SEI 7-22, Reston, VA.

Bridges K, D Cox, S Thomas, S Shin, M Rueben (2011) "Large-scale wave basin experiments on the influence of large obstacles on tsunami inundation forces." Coastal Structures. https://doi.org/10.1142/9789814412216_0107

Bocchiola D, MC Rulli, R Rosso (2006) "Transport of large woody debris in the presence of obstacles." Geomorphology, 76(1–2), 166–178. https://doi.org/10.1016/j.geomorph.2005.08.016

Carden L, G Chock, G Yu, I Robertson (2015) "The new ASCE tsunami design standard applied to mitigate Tohoku tsunami building structural failure mechanisms." Handbook of Coastal Disaster Mitigation for Engineers and Planners, 461–490. https://doi.org/10.1016/b978-0-12-801060-0.00022-8

Chaplin JR, P Teigen (2003) "Steady flow past a vertical surface-piercing circular cylinder." Journal of Fluids and Structures, 18(3–4), 271–285. https://doi.org/10.1016/j.jfluidstructs.2003.07.009

Chock GY (2016) "Design for tsunami loads and effects in the ASCE 7-16 standard." Journal of Structural Engineering, 142(11). https://doi.org/10.1061/(asce)st.1943-541x.0001565

Dibble TL, CK Sollitt (1989) "New designs for acoustic and resistive wave profiles." In Proc., Workshop on Instrumentation for Hydraulic Laboratories, 185–200. Ottawa: International Association for Hydro-Environment Engineering and Research.

Federal Emergency Management Agency (2012) "6. Load Determination and Structural Design Criteria." In Guidelines for Design of Structures for Vertical Evacuation from Tsunamis (Second, pp. 90–91).

Federal Emergency Management Agency (2019) "A. Vertical Evacuation Structure Examples." In Guidelines for Design of Structures for Vertical Evacuation from Tsunamis (Third, pp. A-1).

Fenton JD (2003) "The effects of obstacles on surface levels and boundary resistance in open channels." Proc. 30th IAHR Congress, Thessaloniki, 24-29 August 2003, eds J. Ganoulis and P. Prinos, Vol. C2, pp9-16.

Fritz HM, DA Phillips, A Okayasu, T Shimozono, H Liu, F Mohammed, V Skanavis, CE Synolakis, T Takahashi (2012) "The 2011 Japan tsunami current velocity measurements from survivor videos at Kesennuma Bay Using Lidar." Geophysical Research Letters, 39(7). https://doi.org/10.1029/2011gl050686

Gijón Mancheño A, W Jansen, JC Winterwerp. Predictive model of bulk drag coefficient for a nature-based structure exposed to currents. Sci Rep 11, 3517 (2021). https://doi.org/10.1038/s41598-021-83035-0

Ikeno M, D Takabatake, N Kihara, H Kaida, Y Miyagawa, A Shibayama (2016) "Improvement of collision force formula for woody debris by airborne and hydraulic experiments." Coastal Engineering Journal, 58(4). https://doi.org/10.1142/s0578563416400222

Ko HT-S, DT Cox, HR Riggs, CJ Naito (2015) "Hydraulic experiments on impact forces from tsunami-driven debris." Journal of Waterway, Port, Coastal, and Ocean Engineering, 141(3). https://doi.org/10.1061/(asce)ww.1943-5460.0000286

Matsutomi H, K Okamoto (2010) "Inundation flow velocity of tsunami on land." Island Arc, 19(3), 443–457. https://doi.org/10.1111/j.1440-1738.2010.00725.x

Mauti G, J Stolle, T Takabatake, I Nistor, N Goseberg, A Mohammadian (2020) "Experimental investigation of loading due to debris dams on structures." Journal of Hydraulic Engineering, 146(5). https://doi.org/10.1061/(asce)hy.1943-7900.0001731

Naito C, C Cercone, HR Riggs, D Cox (2014) "Procedure for site assessment of the potential for Tsunami Debris Impact." Journal of Waterway, Port, Coastal, and Ocean Engineering, 140(2), 223–232. https://doi.org/10.1061/(asce)ww.1943-5460.0000222

National Academy of Sciences (2012) "Disaster resilience—A national imperative." National Academies Press, Washington, DC.

Nistor I, N Goseberg, J Stolle (2017) "Tsunami-driven debris motion and loads: A critical review." Frontiers in Built Environment, 3. https://doi.org/10.3389/fbuil.2017.00002

Oudenbroek K, N Naderi, J Bricker, Y Yang, C van der Veen, W Uijttewaal, S Moriguchi, S Jonkman (2018) "Hydrodynamic and debris-damming failure of bridge decks and piers in steady flow." Geosciences, 8(11), 409. https://doi.org/10.3390/geosciences8110409

Park H, MJ Koh, DT Cox, MS Alam, S Shin (2021) “Experimental study of debris transport driven by a tsunami-like wave: Application for non-uniform density groups and obstacles.” Coastal Engineering, 166, 103867. https://doi.org/10.1016/j.coastaleng.2021.103867

Qi ZX, I Eames, ER Johnson (2014) "Force acting on a square cylinder fixed in a free-surface channel flow." Journal of Fluid Mechanics, 756, 716–727. https://doi.org/10.1017/jfm.2014.455

Robertson IN, HR Riggs, SC Yim, YL Young (2007) "Lessons from Hurricane Katrina storm surge on bridges and buildings." Journal of Waterway, Port, Coastal, and Ocean Engineering, 133(6), 463–483. https://doi.org/10.1061/(asce)0733-950x(2007)133:6(463)

Saatcioglu M, A Ghobarah, I Nistor (2005) "Effects of the December 26, 2004 Sumatra Earthquake and Tsunami on Physical Infrastructure." ISET Journal of Earthquake Technology, 42(4), 79–94.

Schmocker L, WH Hager (2011) "Probability of drift blockage at bridge decks." Journal of Hydraulic Engineering, 137(4), 470–479. https://doi.org/10.1061/(asce)hy.1943-7900.0000319

Shekhar K, AO Winter, MS Alam, P Arduino, GR Miller, MR Motley, MO Eberhard, AR Barbosa, P Lomonaco, DT Cox (2020) "Conceptual evaluation of tsunami debris field damming and impact forces." Journal of Waterway, Port, Coastal, and Ocean Engineering, 146(6). https://doi.org/10.1061/(asce)ww.1943-5460.0000600

Stolle J, T Takabatake, I Nistor, T Mikami, S Nishizaki, G Hamano, H Ishii, T Shibayama, N Goseberg, E Petriu (2018) "Experimental investigation of debris damming loads under transient supercritical flow conditions." Coastal Engineering, 139, 16–31. https://doi.org/10.1016/j.coastaleng.2018.04.026

Stolle J, C Krautwald, I Robertson, H Achiari, T Mikami, R Nakamura, T Takabatake, Y Nishida, T Shibayama, M Esteban, I Nistor, N Goseberg (2020) "Engineering lessons from the 28 September 2018 Indonesian tsunami: Debris Loading." Canadian Journal of Civil Engineering, 47(1), 1–12. https://doi.org/10.1139/cjce-2019-0049

Wüthrich D, C Ylla Arbós, M Pfister, AJ Schleiss (2020) "Effect of debris damming on wave-induced hydrodynamic loads against free-standing buildings with openings." Journal of Waterway, Port, Coastal, and Ocean Engineering, 146(1). https://doi.org/10.1061/(asce)ww.1943-5460.0000541

3. Conclusions

The conclusions presented in Chapter 2 represent initial findings of a multi-year experimental campaign to investigate the mechanisms and resulting forces of tsunami-driven debris damming. A second phase of physical experimentation is scheduled to begin September 2024 and will again take place in the Large Wave Flume (LWF) of the O.H. Hinsdale Wave Research Laboratory (HWRL). Additional work within this campaign aims to better understand (1) the mechanisms that lead to debris damming during tsunamis, (2) the factors that increase structural loading due to debris damming, and (3) the effects of non-homogeneous debris on resulting debris dams and loads. Dissemination of the findings of this research is ongoing, with multiple forthcoming publications and presentations.

In addition to the manuscript presented here in Chapter 2, the following publications are anticipated from collaborators:

- Jayasekara JR, S Kameshwar, (2024). *Non-deterministic Kriging for probabilistic systems with mixed continuous and discrete input variables* [to be submitted to *ASCE-ASME Journal of Risk and Uncertainty in Engineering Systems, Part A: Civil Engineering*].
- Koh M, H Park, R Jayasekara, K Doyle, S Kameshwar, D Cox, P Lomonaco (2024). *Experimental modeling of tsunami-driven debris damming loads on a coastal column structure* [to be submitted to *Coastal Engineering*].
- Jayasekara JR, S Kameshwar, (2024). *A sequential design strategy based on non-deterministic Kriging and subset simulations for probabilistic systems with mixed continuous and discrete input variables* [publication to be determined].

Findings from this experimental campaign have been/will be presented by collaborators in the following settings:

- ASCE Engineering Mechanics Institute Conference, June 2023, Atlanta, Georgia (USA), presented by Ravindu Jayasekara
- Ocean Sciences Meeting, February 2024, New Orleans, Louisiana (USA), presented by Myung-Jin Koh

- Coastlab24, May 2024, Delft (Netherlands), presented by Kellen Doyle
- ASCE Engineering Mechanics Institute and Probabilistic Mechanics & Reliability Conference, May 2024, Chicago, Illinois (USA), presented by Ravindu Jayasekara
- Young Coastal Scientists and Engineers Conference, June 2024, Québec (Canada), presented by Ravindu Jayasekara
- International Conference on Coastal Engineering, September 2024, Rome (Italy), presented by Dr. Pedro Lomonaco

Bibliography

Aghl PI, CJ Naito, HR Riggs (2015) "Estimation of demands resulting from inelastic axial impact of steel debris." Engineering Structures, 82, 11–21. https://doi.org/10.1016/j.engstruct.2014.10.021

Arnason H, C Petroff, H Yeh (2009) "Tsunami bore impingement onto a vertical column." Journal of Disaster Research, 4(6), 391–403. https://doi.org/10.20965/jdr.2009.p0391

ASCE/SEI (2016) "Minimum design loads for buildings and other structures." ASCE/SEI 7-16, Reston, VA.

ASCE/SEI (2022) "Minimum design loads for buildings and other structures." ASCE/SEI 7-22, Reston, VA.

Bridges K, D Cox, S Thomas, S Shin, M Rueben (2011) "Large-scale wave basin experiments on the influence of large obstacles on tsunami inundation forces." Coastal Structures. https://doi.org/10.1142/9789814412216_0107

Bocchiola D, MC Rulli, R Rosso (2006) "Transport of large woody debris in the presence of obstacles." Geomorphology, 76(1–2), 166–178. https://doi.org/10.1016/j.geomorph.2005.08.016

Carden L, G Chock, G Yu, I Robertson (2015) "The new ASCE tsunami design standard applied to mitigate Tohoku tsunami building structural failure mechanisms." Handbook of Coastal Disaster Mitigation for Engineers and Planners, 461–490. https://doi.org/10.1016/b978-0-12-801060-0.00022-8

Chaplin JR, P Teigen (2003) "Steady flow past a vertical surface-piercing circular cylinder." Journal of Fluids and Structures, 18(3–4), 271–285. https://doi.org/10.1016/j.jfluidstructs.2003.07.009

Chida Y, N Mori (2023). Numerical modeling of debris transport due to tsunami flow in a coastal urban area. Coastal Engineering, 179, 104243. https://doi.org/10.1016/j.coastaleng.2022.104243

Chock GY (2016) "Design for tsunami loads and effects in the ASCE 7-16 standard." Journal of Structural Engineering, 142(11). https://doi.org/10.1061/(asce)st.1943-541x.0001565

Dibble TL, CK Sollitt (1989) "New designs for acoustic and resistive wave profiles." In Proc., Workshop on Instrumentation for Hydraulic Laboratories, 185–200. Ottawa: International Association for Hydro-Environment Engineering and Research.

Federal Emergency Management Agency (2012) "6. Load Determination and Structural Design Criteria." In Guidelines for Design of Structures for Vertical Evacuation from Tsunamis (Second, pp. 90–91).

Federal Emergency Management Agency (2019) "A. Vertical Evacuation Structure Examples." In Guidelines for Design of Structures for Vertical Evacuation from Tsunamis (Third, pp. A-1).

Fenton JD (2003) "The effects of obstacles on surface levels and boundary resistance in open channels." Proc. 30th IAHR Congress, Thessaloniki, 24-29 August 2003, eds J. Ganoulis and P. Prinos, Vol. C2, pp9-16.

Fritz HM, DA Phillips, A Okayasu, T Shimozono, H Liu, F Mohammed, V Skanavis, CE Synolakis, T Takahashi (2012) "The 2011 Japan tsunami current velocity measurements from survivor videos at Kesennuma Bay Using Lidar." Geophysical Research Letters, 39(7). https://doi.org/10.1029/2011gl050686

Gijón Mancheño A, W Jansen, JC Winterwerp. Predictive model of bulk drag coefficient for a nature-based structure exposed to currents. Sci Rep 11, 3517 (2021). https://doi.org/10.1038/s41598-021-83035-0

Gupta A, A Heidarpour, MR Behera (2022). Effect of structure orientation and debris initial orientation on peak debris loading during tsunami: An experimental and Numerical Investigation. Applied Ocean Research, 121, 103075. https://doi.org/10.1016/j.apor.2022.103075

Ikeno M, D Takabatake, N Kihara, H Kaida, Y Miyagawa, A Shibayama (2016) "Improvement of collision force formula for woody debris by airborne and hydraulic experiments." Coastal Engineering Journal, 58(4). https://doi.org/10.1142/s0578563416400222

Ko HT-S, DT Cox, HR Riggs, CJ Naito (2015) "Hydraulic experiments on impact forces from tsunami-driven debris." Journal of Waterway, Port, Coastal, and Ocean Engineering, 141(3). https://doi.org/10.1061/(asce)ww.1943-5460.0000286

Mascarenas D, M Motley, M Eberhard, P Arduino, A Serrone (2022). Quantifying and understanding structural loading from wave-driven debris fields. Ports 2022. https://doi.org/10.1061/9780784484395.052

Matsutomi H, K Okamoto (2010) "Inundation flow velocity of tsunami on land." Island Arc, 19(3), 443–457. https://doi.org/10.1111/j.1440-1738.2010.00725.x

Mauti G, J Stolle, T Takabatake, I Nistor, N Goseberg, A Mohammadian (2020) "Experimental investigation of loading due to debris dams on structures." Journal of Hydraulic Engineering, 146(5). https://doi.org/10.1061/(asce)hy.1943-7900.0001731

Naito C, C Cercone, HR Riggs, D Cox (2014) "Procedure for site assessment of the potential for Tsunami Debris Impact." Journal of Waterway, Port, Coastal, and Ocean Engineering, 140(2), 223–232. https://doi.org/10.1061/(asce)ww.1943-5460.0000222

National Academy of Sciences (2012) "Disaster resilience—A national imperative." National Academies Press, Washington, DC.

Nistor I, N Goseberg, J Stolle (2017) "Tsunami-driven debris motion and loads: A critical review." Frontiers in Built Environment, 3. https://doi.org/10.3389/fbuil.2017.00002

Oudenbroek K, N Naderi, J Bricker, Y Yang, C van der Veen, W Uijttewaal, S Moriguchi, S Jonkman (2018) "Hydrodynamic and debris-damming failure of bridge decks and piers in steady flow." Geosciences, 8(11), 409. https://doi.org/10.3390/geosciences8110409

Park H, MJ Koh, DT Cox, MS Alam, S Shin (2021) “Experimental study of debris transport driven by a tsunami-like wave: Application for non-uniform density groups and obstacles.” Coastal Engineering, 166, 103867. https://doi.org/10.1016/j.coastaleng.2021.103867

Qi ZX, I Eames, ER Johnson (2014) "Force acting on a square cylinder fixed in a free-surface channel flow." Journal of Fluid Mechanics, 756, 716–727. https://doi.org/10.1017/jfm.2014.455

Robertson IN, HR Riggs, SC Yim, YL Young (2007) "Lessons from Hurricane Katrina storm surge on bridges and buildings." Journal of Waterway, Port, Coastal, and Ocean Engineering, 133(6), 463–483. https://doi.org/10.1061/(asce)0733-950x(2007)133:6(463)

Saatcioglu M, A Ghobarah, I Nistor (2005) "Effects of the December 26, 2004 Sumatra Earthquake and Tsunami on Physical Infrastructure." ISET Journal of Earthquake Technology, 42(4), 79–94.

Schmocker L, WH Hager (2011) "Probability of drift blockage at bridge decks." Journal of Hydraulic Engineering, 137(4), 470–479. https://doi.org/10.1061/(asce)hy.1943-7900.0000319

Shekhar K, AO Winter, MS Alam, P Arduino, GR Miller, MR Motley, MO Eberhard, AR Barbosa, P Lomonaco, DT Cox (2020) "Conceptual evaluation of tsunami debris field damming and impact forces." Journal of Waterway, Port, Coastal, and Ocean Engineering, 146(6). https://doi.org/10.1061/(asce)ww.1943-5460.0000600

Schlesier, H G., H von Häfen, N Goseberg (2021). Physical modelling of tsunami barrier and debris interaction. Journal of Coastal and Hydraulic Structures. https://doi.org/10.48438/jchs.2021.0003

Stolle J, T Takabatake, I Nistor, T Mikami, S Nishizaki, G Hamano, H Ishii, T Shibayama, N Goseberg, E Petriu (2018) "Experimental investigation of debris damming loads under transient supercritical flow conditions." Coastal Engineering, 139, 16–31. https://doi.org/10.1016/j.coastaleng.2018.04.026

Stolle J, C Krautwald, I Robertson, H Achiari, T Mikami, R Nakamura, T Takabatake, Y Nishida, T Shibayama, M Esteban, I Nistor, N Goseberg (2020) "Engineering lessons from the 28 September 2018 Indonesian tsunami: Debris Loading." Canadian Journal of Civil Engineering, 47(1), 1–12. https://doi.org/10.1139/cjce-2019-0049

Wüthrich D, C Ylla Arbós, M Pfister, AJ Schleiss (2020) "Effect of debris damming on wave-induced hydrodynamic loads against free-standing buildings with openings." Journal of Waterway, Port, Coastal, and Ocean Engineering, 146(1). https://doi.org/10.1061/(asce)ww.1943-5460.0000541

APPENDICES

Appendix A Incident Wave Conditions

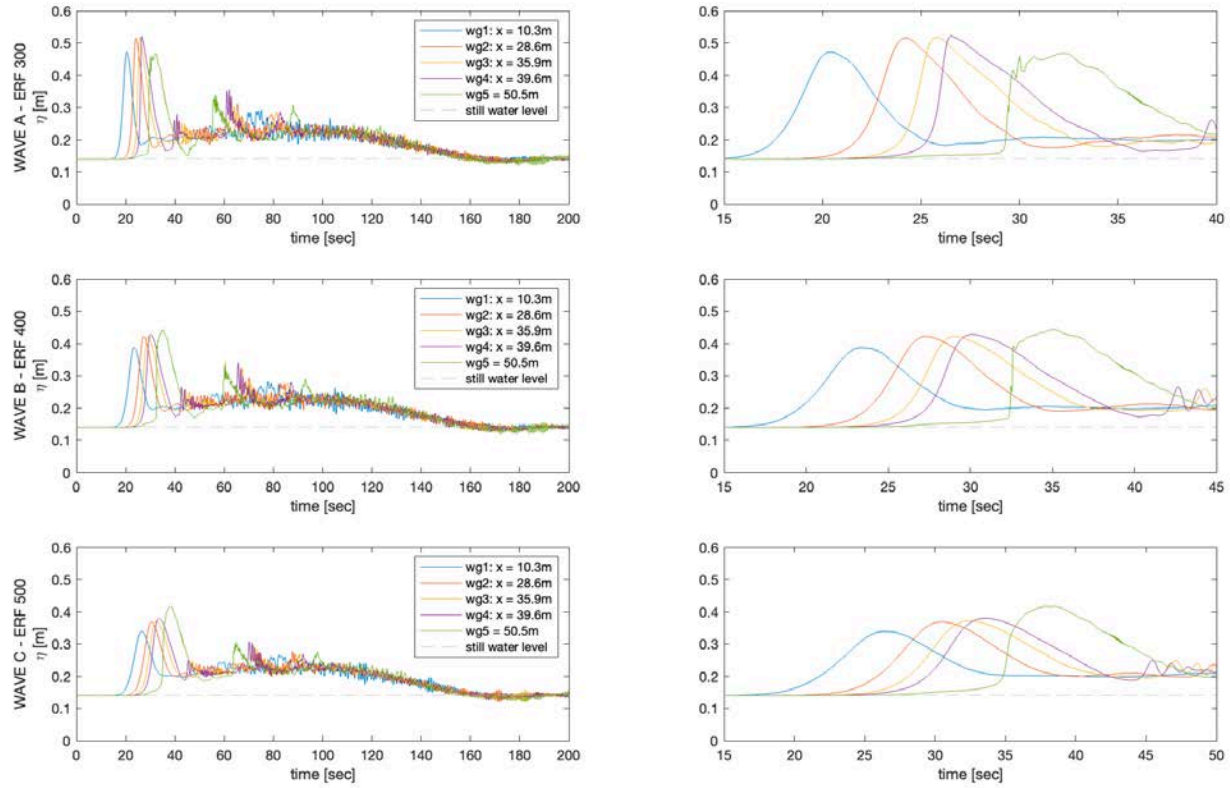

Figure A.1. Free-surface elevations as measured by resistance wave gauges (wg). Data shown for each incident wave condition, full test duration (left) and isolated inundation phase (right).

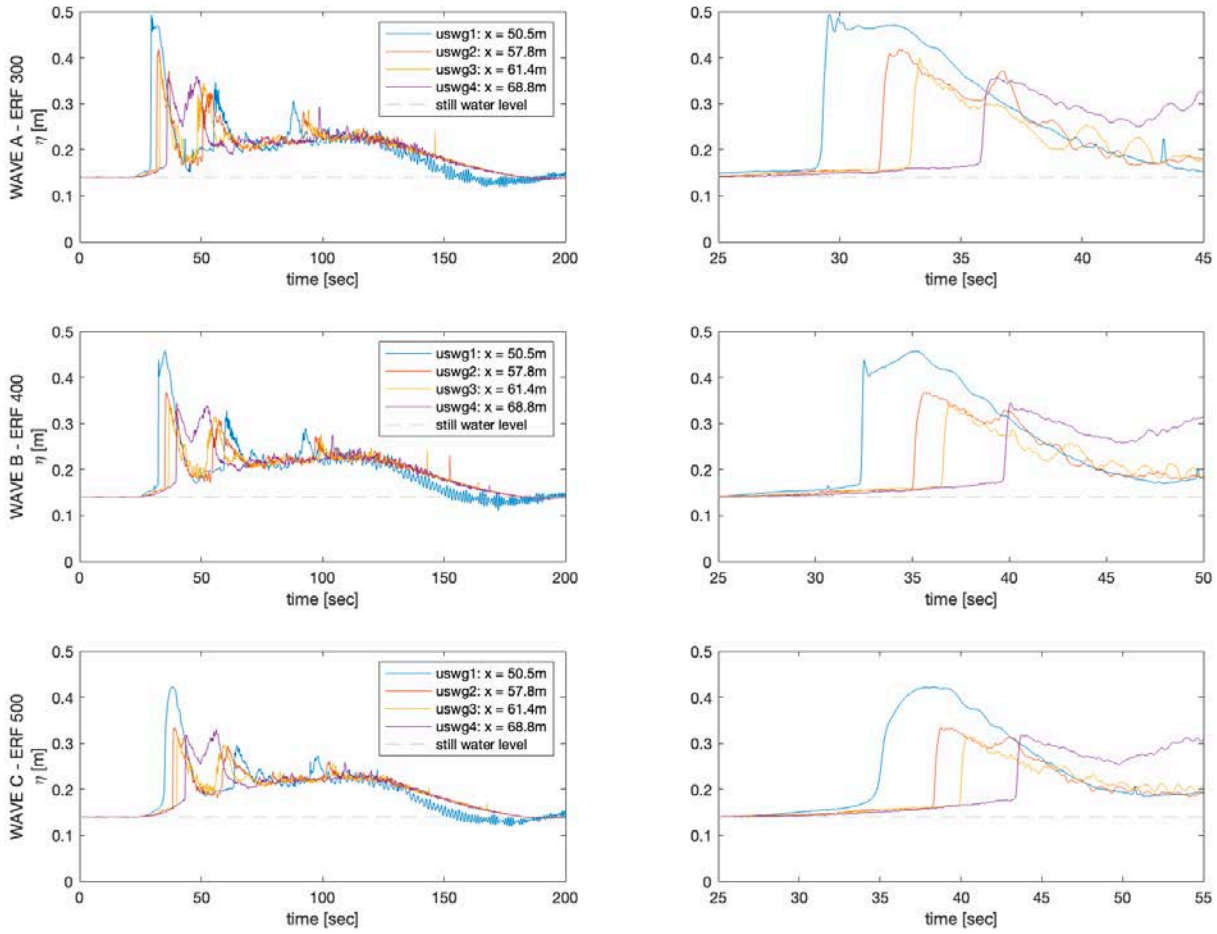

Figure A.2. Free-surface elevations as measured by ultrasonic wave gauges (uswg). Data shown for each incident wave condition, full test duration (left) and isolated inundation phase (right).

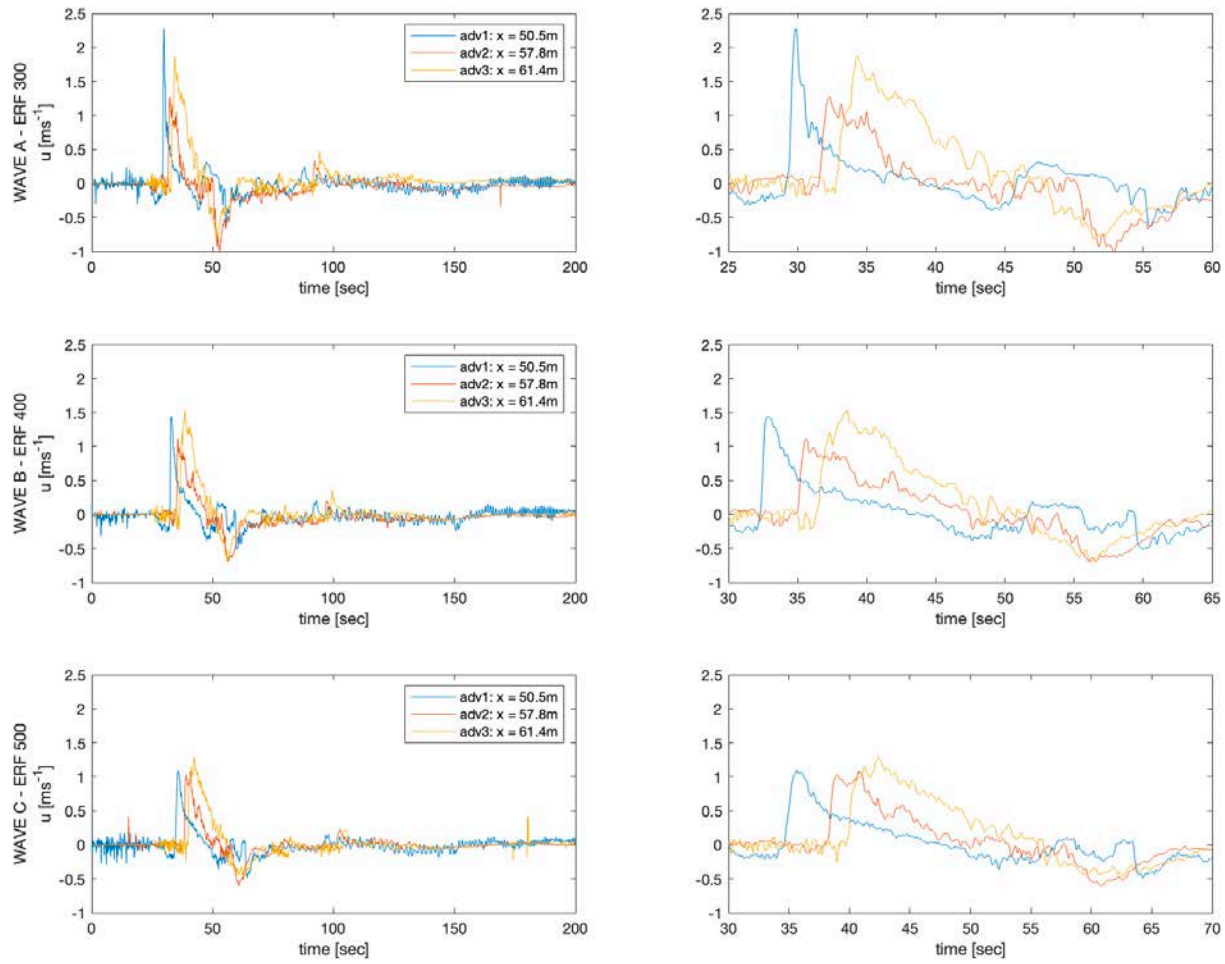

Figure A.3. Flow velocities as measured by acoustic doppler velocimeters (adv). Data shown for each incident wave condition, full test duration (left) and isolated inundation phase (right).

Appendix B – Debris Element Catalog

Table A.1. Inventory of 1:20-scale 6.1 m (20 ft) shipping container debris elements.

Element #	IMU *Yes/No*	Length *(cm)*	Width *(cm)*	Height *(cm)*	Mass *(kg)*	Density *(kg/m^3)*
1	N	29.9	11.5	11.5	2.054	519.4
2	N	29.8	11.4	11.5	2.254	576.9
3	N	29.9	11.3	11.3	2.158	565.2
4	N	29.9	11.3	11.5	2.480	638.3
5	Y	29.9	11.5	11.4	2.352	600.0
6	N	30.0	11.3	11.2	2.324	612.1
7	N	30.0	11.4	11.4	2.174	557.6
8	N	29.8	11.4	11.5	2.270	581.0
9	N	30.0	11.4	11.5	2.264	575.6
10	Y	29.7	11.4	11.4	2.112	547.2
11	N	29.9	11.5	11.5	2.062	521.5
12	N	30.0	11.3	11.3	2.098	547.7
13	N	30.0	11.5	11.3	2.084	534.6
14	Y	30.0	11.4	11.3	2.116	547.5
15	N	30.0	11.3	11.1	2.120	563.4
16	N	29.8	11.4	11.3	2.164	563.7
17	N	29.9	11.5	11.4	2.176	555.1
18	N	30.0	11.2	11.2	2.168	576.1
19	N	29.9	11.3	11.4	2.046	531.2
20	N	29.8	11.4	11.4	2.042	527.3
21	Y	29.9	11.4	11.4	2.056	529.1
22	N	29.9	11.3	11.4	2.184	567.0
23	Y	29.9	11.3	11.4	2.074	538.5

Table A.2. Inventory of 1:20-scale 12.2 m (40 ft) shipping container debris elements.

Element #	IMU *Yes/No*	Length *(cm)*	Width *(cm)*	Height *(cm)*	Mass *(kg)*	Density *(kg/m^3)*
1	N	59.7	11.2	11.3	4.212	557.5
2	Y	59.9	11.2	11.3	4.284	565.1
3	Y	60.0	11.4	11.5	4.558	579.5
4	N	59.7	11.4	11.5	4.250	543.0
5	N	59.7	11.3	11.3	4.034	529.2
6	Y	59.8	11.4	11.4	4.308	554.3
7	N	59.8	11.3	11.4	4.046	525.2
8	N	60.0	11.3	11.4	4.122	533.3
9	Y	59.8	11.5	11.6	4.104	514.5
10	Y	59.8	11.5	11.5	4.204	531.6

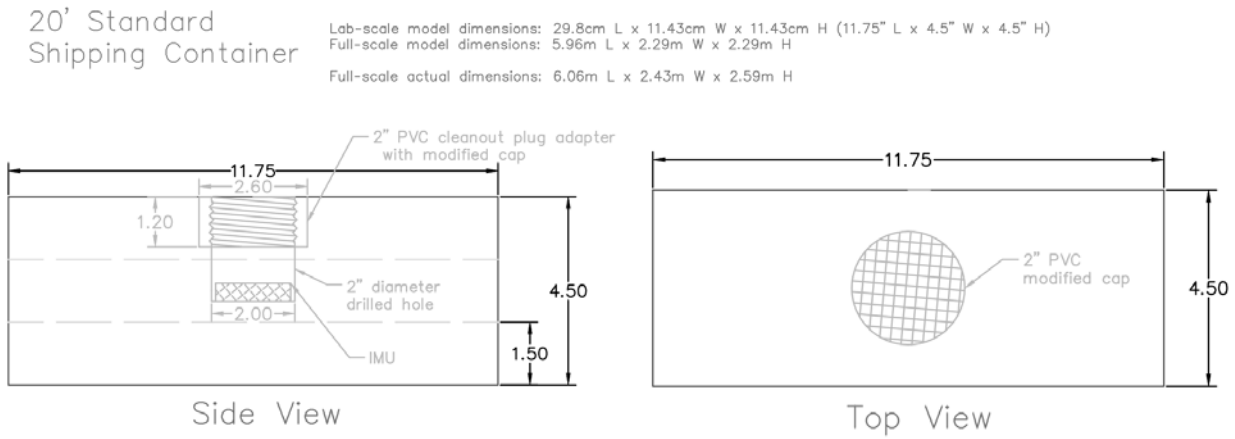

Fig A.4. Fabrication specification of 1:20-scale 6.1 m (20 ft) shipping container debris elements.

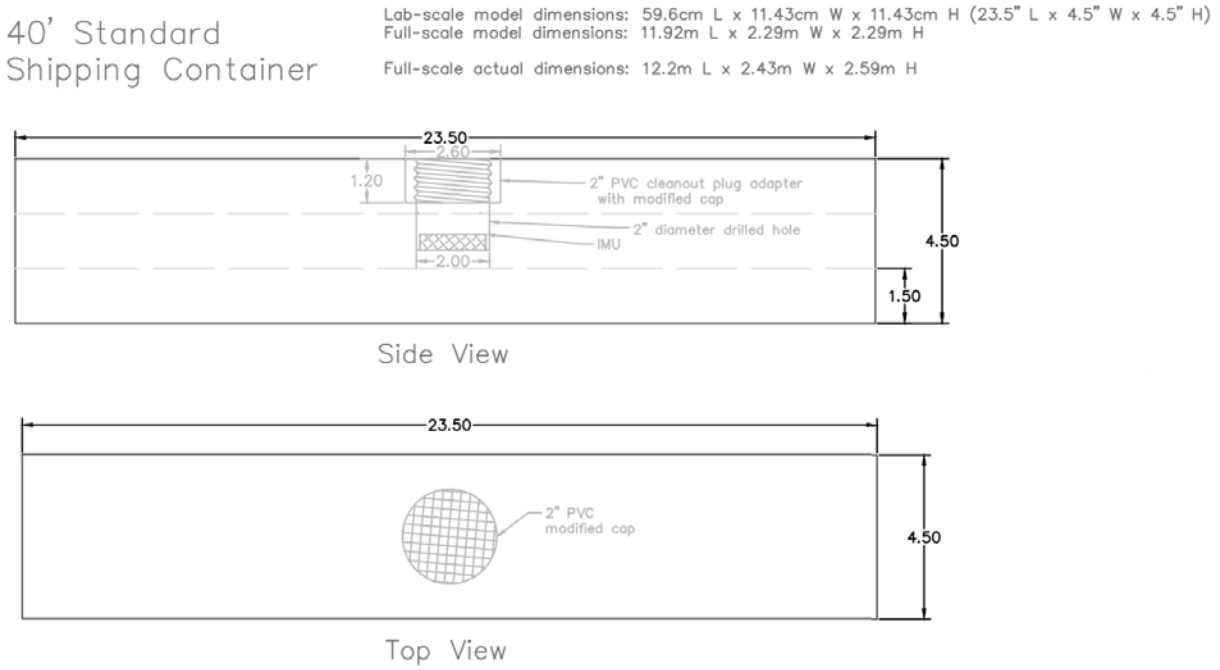

Fig A.5. Fabrication specification of 1:20-scale 12.2 m (40 ft) shipping container debris elements.

Appendix C – Photogrammetry Archetypes

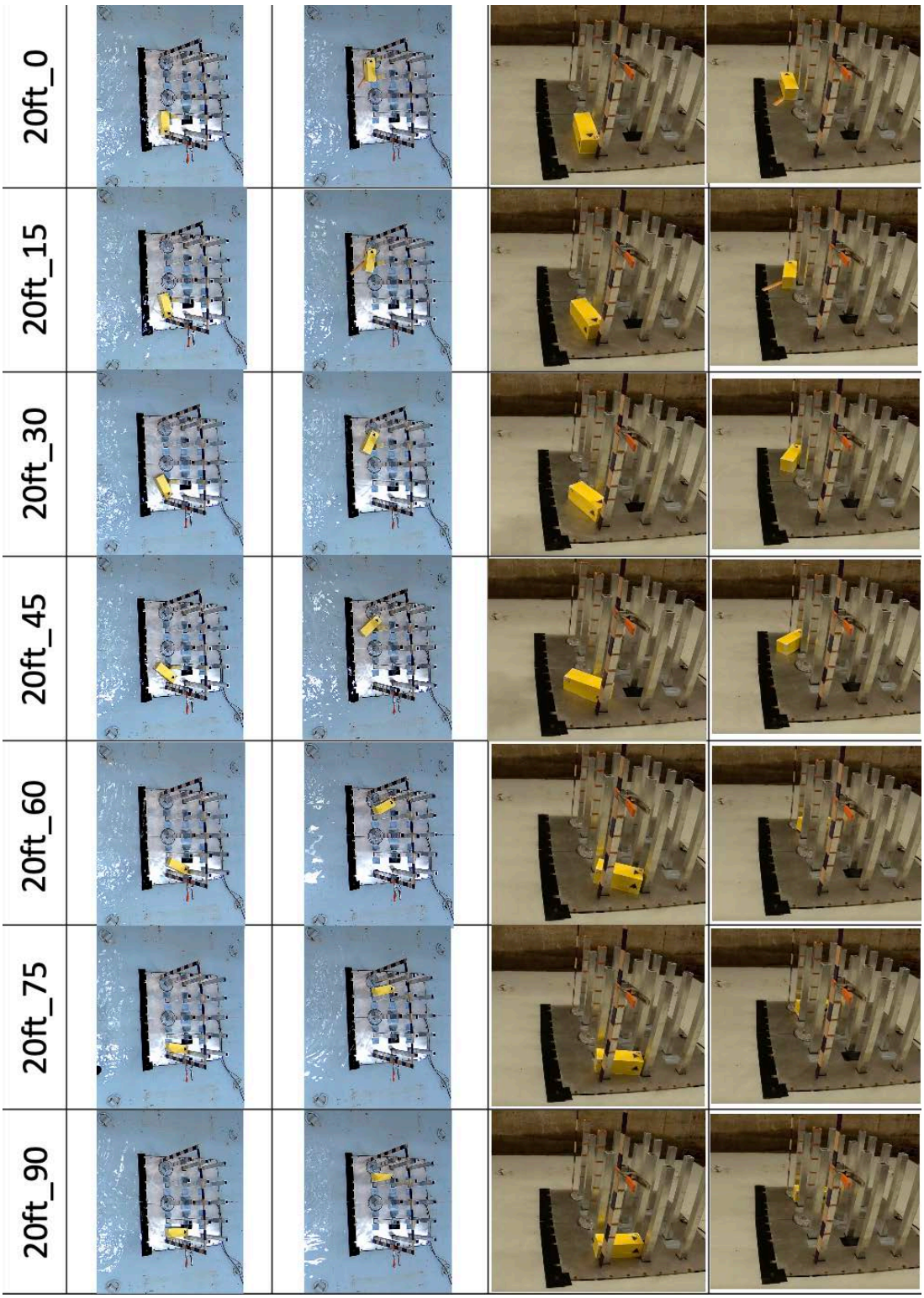

Figure A.6. Archetype images for 6.1 m (20 ft) shipping containers. Used to estimate damming angle in photogrammetric method; plan view (left) and isometric view (right).

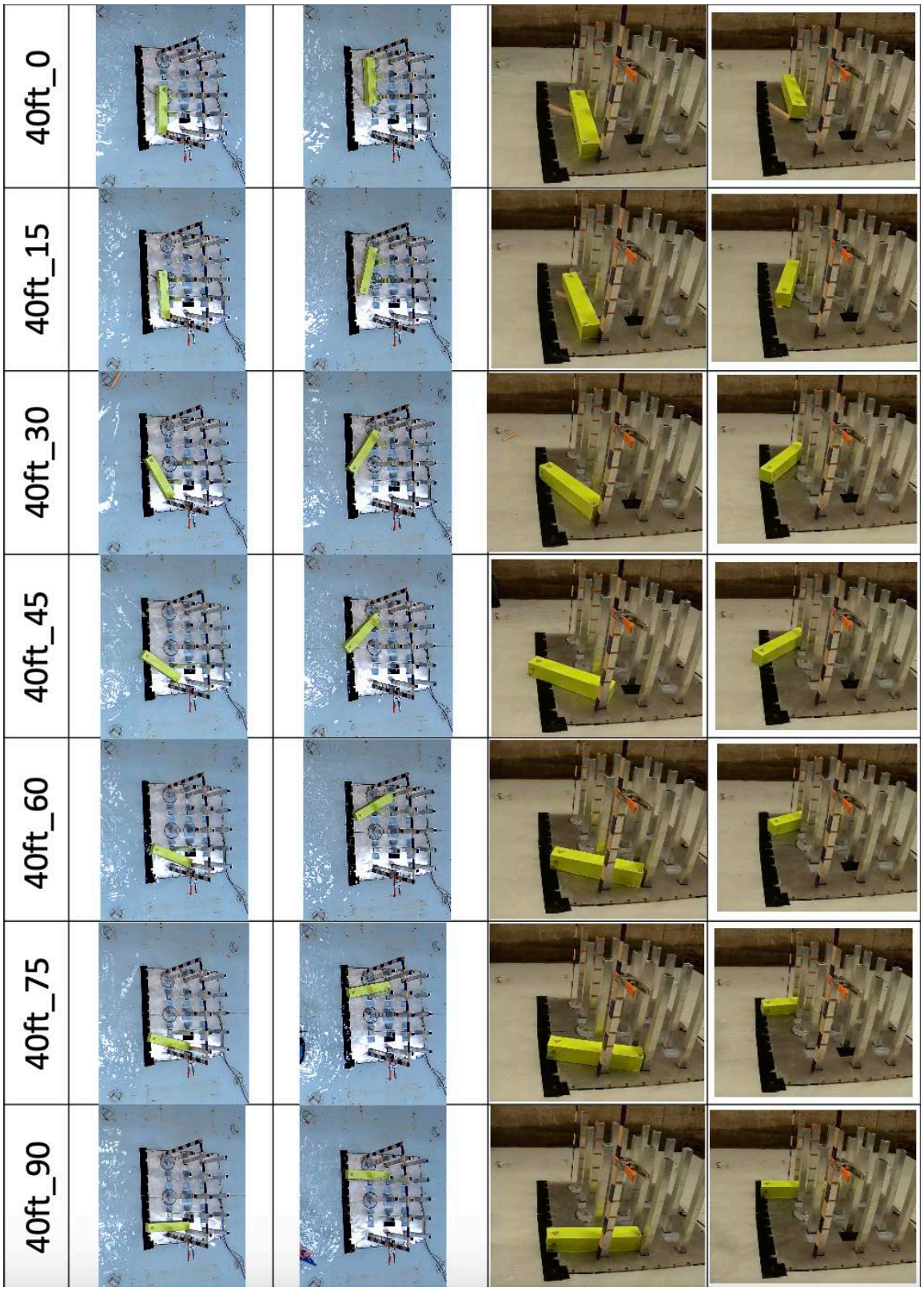

Figure A.7. Archetype images for 12.2 m (40 ft) shipping containers. Used to estimate damming angle in photogrammetric method; plan view (left) and isometric view (right).

Appendix D – Photogrammetry Method Validation and Error Analysis

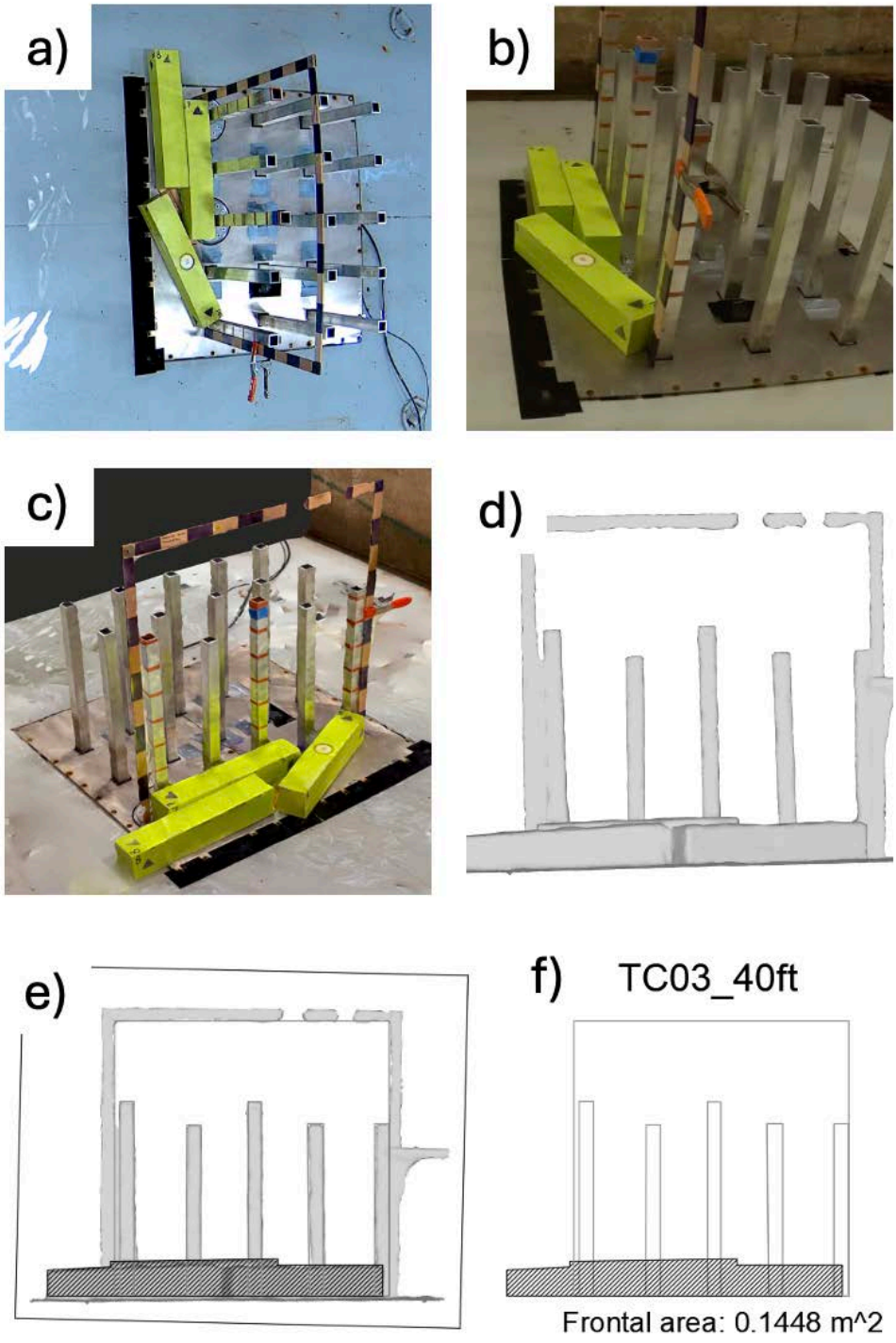

Fig A.8. Example photogrammetry method validation test case; (a) CCTV plan view, (b) GoPro isometric view, (c) rendered .obj file, (d) flow-aligned orthographic projection, (e) re-scaled and annotated projection in AutoCAD, (f) idealized projection with measured area of test case.

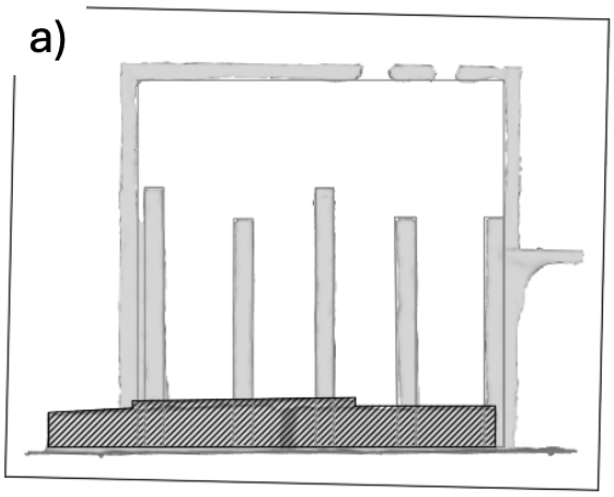

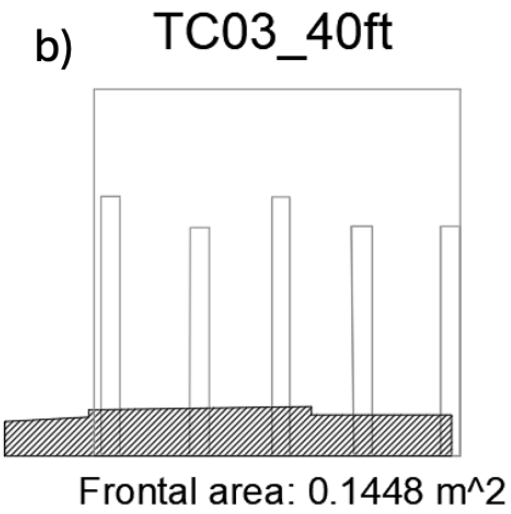

c)

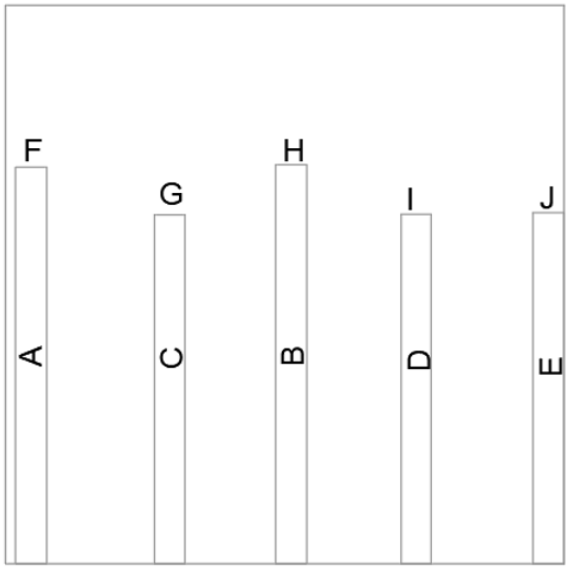

d)

Dim	CAD est.	Measured	% diff
C	0.6245	0.63	-0.9%
D	0.6258	0.63	-0.7%
E	0.6286	0.63	-0.2%
A	0.7102	0.712	-0.3%
B	0.7145	0.712	0.4%
F	0.056	0.052	7.7%
G	0.0546	0.052	5.0%
H	0.0559	0.052	7.5%
I	0.0532	0.052	2.3%
J	0.0552	0.052	6.2%
		Avg length error	2.7%

Fig A.9. Error quantification of CAD-based test case measurement; (a) re-scaled and annotated projection in AutoCAD, (b) idealized projection with measured area of test case, (c) dimensions used in error analysis, (d) error analysis comparing CAD-estimated and manually-measured dimensions shown in (c).

Appendix E – Analyzed Experimental Debris Dams

Table A.3. Summary of analyzed experimental debris dam test parameters.

Dam ID	Video ID	Region *impact or quasi-static*	Wave *ERF scale*	Column array *# R x # C*	Debris *SC size (m)*
1	0427_T02_ERF400_LT15_D03	I	400	3x7	6.1
2	0427_T02_ERF400_LT15_D03	QS	400	3x7	6.1
3	0427_T03_ERF300_LT15_D03	I	300	3x7	6.1
4	0427_T03_ERF300_LT15_D03	QS	300	3x7	6.1
5	0427_T04_ERF500_LT15_D03	QS	500	3x7	6.1
6	0427_T06_ERF300_LT15_D04	I	300	3x7	6.1
7	0427_T06_ERF300_LT15_D04	QS	300	3x7	6.1
8	0427_T07_ERF500_LT20_D02	I	500	3x7	6.1
9	0427_T14_ERF400_LF10_D09	I	400	3x7	12.2
10	0427_T14_ERF400_LF10_D09	QS	400	3x7	12.2
11	0504_T04_ERF500_LF10_D02	I	500	3x3	12.2
12	0504_T04_ERF500_LF10_D02	QS	500	3x3	12.2
13	0504_T06_ERF300_LF10_D04	I	300	3x3	12.2
14	0504_T06_ERF300_LF10_D04	QS	300	3x3	12.2
15	0427_T20_ERF300_LF10_D01	QS	300	3x7	12.2
16	0504_T07_ERF400_LF10_D05	I	400	3x3	12.2
17	0504_T07_ERF400_LF10_D05	QS	400	3x3	12.2
18	0505_T01_ERF500_LF10_D01	I	500	3x3	12.2
19	0505_T02_ERF400_LF10_D01	I	400	3x3	12.2
20	0505_T02_ERF400_LF10_D01	QS	400	3x3	12.2
21	0505_T03_ERF300_LF10_D00	I	300	3x3	12.2
22	0505_T05_ERF400_LF10_D01	QS	400	3x3	12.2
23	0502_T08_ERF400_LF10_D01	QS	400	3x7	12.2
24	0505_T08_ERF400_LF10_D08	I	400	3x3	12.2
25	0505_T08_ERF400_LF10_D08	QS	400	3x3	12.2
26	0505_T13_ERF400_LF10_D04	I	400	3x3	12.2
27	0505_T13_ERF400_LF10_D04	QS	400	3x3	12.2
28	0505_T16_ERF500_LF10_D03	I	500	3x3	12.2
29	0505_T17_ERF500_LF10_D04	I	500	3x3	12.2
30	0505_T17_ERF500_LF10_D04	QS	500	3x3	12.2
31	0510_T04_ERF500_LF10_D07	QS	500	3x5	12.2
32	0510_T06_ERF300_LF10_D05	I	300	3x5	12.2
33	0510_T06_ERF300_LF10_D05	QS	300	3x5	12.2

Table A.3. Summary of analyzed experimental debris dam test parameters. (Continued)

34	0510_T07_ERF500_LF10_D08	QS	500	3x5	12.2
35	0510_T08_ERF400_LF10_D09	QS	400	3x5	12.2
36	0510_T13_ERF500_LF10_D04	I	500	3x5	12.2
37	0510_T13_ERF500_LF10_D04	QS	500	3x5	12.2
38	0510_T14_ERF400_LF10_D02	QS	400	3x5	12.2
39	0510_T15_ERF300_LF10_D03	I	300	3x5	12.2
40	0510_T15_ERF300_LF10_D03	QS	300	3x5	12.2
41	0510_T17_ERF400_LF10_D02	I	400	3x5	12.2
42	0510_T17_ERF400_LF10_D02	QS	400	3x5	12.2
43	0511_T01_ERF500_LT15_D03	I	500	3x5	6.1
44	0511_T01_ERF500_LT15_D03	QS	500	3x5	6.1
45	0511_T02_ERF400_LT15_D03	I	400	3x5	6.1
46	0511_T02_ERF400_LT15_D03	QS	400	3x5	6.1
47	0511_T03_ERF300_LT15_D02	I	300	3x5	6.1
48	0511_T03_ERF300_LT15_D02	QS	300	3x5	6.1
49	0511_T07_ERF500_LT15_D06	I	500	3x5	6.1
50	0511_T07_ERF500_LT15_D06	QS	500	3x5	6.1
51	0511_T08_ERF400_LT15_D04	I	400	3x5	6.1
52	0511_T08_ERF400_LT15_D04	QS	400	3x5	6.1
53	0511_T09_ERF300_LT15_D01	I	300	3x5	6.1
54	0511_T09_ERF300_LT15_D01	QS	300	3x5	6.1
55	0511_T12_ERF300_LT15_D03	QS	300	3x5	6.1
56	0511_T14_ERF400_LT15_D04	I	400	3x5	6.1
57	0511_T14_ERF400_LT15_D04	QS	400	3x5	6.1
58	0511_T15_ERF300_LT15_D04	I	300	3x5	6.1
59	0511_T15_ERF300_LT15_D04	QS	300	3x5	6.1
60	0511_T16_ERF500_LT15_D02	I	500	3x5	6.1
61	0511_T16_ERF500_LT15_D02	QS	500	3x5	6.1
62	0511_T17_ERF400_LT15_D03	I	400	3x5	6.1
63	0511_T17_ERF400_LT15_D03	QS	400	3x5	6.1
64	0515_T02_ERF400_LT15_D01	I	400	3x3	6.1
65	0515_T02_ERF400_LT15_D01	QS	400	3x3	6.1
66	0505_T06_ERF300_LF10_D05	I	300	3x3	12.2
67	0505_T06_ERF300_LF10_D05	QS	300	3x3	12.2
68	0505_T09_ERF300_LF10_D02	I	300	3x3	12.2
69	0505_T09_ERF300_LF10_D02	QS	300	3x3	12.2
70	0427_T09_ERF300_LT20_D03	I	300	3x7	6.1

Table A.3. Summary of analyzed experimental debris dam test parameters. (Continued)

71	0427_T09_ERF300_LT20_D03	QS	300	3x7	6.1
72	0427_T13_ERF500_LF10_D03	QS	500	3x7	12.2
73	0427_T19_ERF400_LF10_D03	I	400	3x7	12.2
74	0427_T19_ERF400_LF10_D03	QS	400	3x7	12.2
75	0505_T07_ERF500_LF10_D01	I	500	3x3	12.2
76	0505_T07_ERF500_LF10_D01	QS	500	3x3	12.2
77	0505_T12_ERF300_LF10_D04	QS	300	3x3	12.2
78	0505_T14_ERF300_LF10_D02	I	300	3x3	12.2
79	0505_T14_ERF300_LF10_D02	QS	300	3x3	12.2
80	0505_T15_ERF400_LF10_D06	QS	400	3x3	12.2
81	0510_T01_ERF500_LF10_D05	QS	500	3x5	12.2
82	0510_T02_ERF400_LF10_D03	I	400	3x5	12.2
83	0510_T02_ERF400_LF10_D03	QS	400	3x5	12.2
84	0510_T03_ERF300_LF10_D05	I	300	3x5	12.2
85	0510_T03_ERF300_LF10_D05	QS	300	3x5	12.2
86	0510_T05_ERF400_LF10_D03	I	400	3x5	12.2
87	0510_T05_ERF400_LF10_D03	QS	400	3x5	12.2
88	0510_T16_ERF500_LF10_D01	QS	500	3x5	12.2
89	0511_T04_ERF500_LT15_D05	I	500	3x5	6.1
90	0511_T04_ERF500_LT15_D05	QS	500	3x5	6.1
91	0511_T05_ERF400_LT15_D03	I	400	3x5	6.1
92	0511_T05_ERF400_LT15_D03	QS	400	3x5	6.1
93	0511_T06_ERF300_LT15_D04	I	300	3x5	6.1
94	0511_T06_ERF300_LT15_D04	QS	300	3x5	6.1
95	0511_T10_ERF500_LT15_D04	QS	500	3x5	6.1
96	0511_T11_ERF400_LT15_D06	I	400	3x5	6.1
97	0511_T11_ERF400_LT15_D06	QS	400	3x5	6.1
98	0511_T13_ERF500_LT15_D04	I	500	3x5	6.1
99	0511_T13_ERF500_LT15_D04	QS	500	3x5	6.1
100	0515_T05_ERF400_LT15_D01	QS	400	3x3	6.1
101	0502_T01_ERF400_LT15_D02	I	400	3x7	6.1
102	0502_T01_ERF400_LT15_D02	QS	400	3x7	6.1
103	0502_T04_ERF400_LT15_D04	I	400	3x7	6.1
104	0502_T04_ERF400_LT15_D04	QS	400	3x7	6.1
105	0502_T05_ERF400_LT15_D03	I	400	3x7	6.1
106	0502_T05_ERF400_LT15_D03	QS	400	3x7	6.1
107	0502_T06_ERF400_LT15_D03	I	400	3x7	6.1

Table A.3. Summary of analyzed experimental debris dam test parameters. (Continued)

108	0502_T06_ERF400_LT15_D03	QS	400	3x7	6.1
109	0502_T07_ERF400_LT15_D04	I	400	3x7	6.1
110	0502_T07_ERF400_LT15_D04	QS	400	3x7	6.1
111	0502_T08_ERF400_LF10_D01	QS	400	3x7	12.2
112	0502_T10_ERF400_LF10_D01	QS	400	3x7	12.2
113	0502_T12_ERF400_LF10_D03	I	400	3x7	12.2
114	0502_T12_ERF400_LF10_D03	QS	400	3x7	12.2
115	0502_T13_ERF400_LF10_D05	I	400	3x7	12.2
116	0502_T13_ERF400_LF10_D05	QS	400	3x7	12.2

Table A.4. Summary of analyzed experimental debris dam hydrodynamic values.

Dam ID	Time *[sec]*	Depth *[m]*	Velocity *[m/s]*	Fr *[-]*
1	38.46	0.164	1.030	0.839
2	41.41	0.121	0.659	0.633
3	34.78	0.183	1.186	0.882
4	35.80	0.160	1.132	0.912
5	43.81	0.132	0.735	0.682
6	34.45	0.198	1.256	0.937
7	37.82	0.120	0.524	0.585
8	44.53	0.124	0.640	0.598
9	39.26	0.146	1.042	0.889
10	41.76	0.118	0.643	0.620
11	44.68	0.118	0.643	0.609
12	45.83	0.103	0.494	0.496
13	35.89	0.156	1.091	0.891
14	38.80	0.098	0.417	0.424
15	37.17	0.138	0.835	0.822
16	39.85	0.134	0.856	0.766
17	41.30	0.121	0.661	0.634
18	46.30	0.091	0.444	0.475
19	40.09	0.131	0.792	0.735
20	41.44	0.120	0.660	0.635
21	34.40	0.198	1.270	0.945
22	40.01	0.131	0.804	0.737
23	41.00	0.124	0.712	0.679
24	39.89	0.135	0.875	0.775
25	42.19	0.114	0.529	0.513
26	40.25	0.129	0.804	0.760
27	42.13	0.113	0.524	0.506
28	45.91	0.101	0.488	0.495
29	44.07	0.131	0.689	0.641
30	44.49	0.125	0.647	0.603
31	44.03	0.132	0.712	0.660
32	36.41	0.142	0.933	0.817
33	37.99	0.113	0.525	0.578
34	46.44	0.088	0.451	0.490
35	40.55	0.128	0.725	0.685
36	44.41	0.125	0.650	0.604

Table A.4. Summary of analyzed experimental debris dam hydrodynamic values. (Continued)

37	47.13	0.085	0.394	0.438
38	38.90	0.153	1.051	0.864
39	35.31	0.172	1.173	0.908
40	38.48	0.101	0.491	0.529
41	40.77	0.128	0.767	0.726
42	41.84	0.117	0.644	0.619
43	42.98	0.137	0.768	0.684
44	44.03	0.131	0.691	0.644
45	37.78	0.177	1.102	0.838
46	39.80	0.136	0.890	0.782
47	32.93	0.249	1.057	0.740
48	35.03	0.179	1.203	0.922
49	42.40	0.142	0.877	0.769
50	45.40	0.111	0.578	0.564
51	38.79	0.155	1.066	0.871
52	39.74	0.137	0.915	0.801
53	35.26	0.172	1.166	0.901
54	36.36	0.144	0.975	0.856
55	35.36	0.173	1.175	0.917
56	38.64	0.162	1.019	0.827
57	39.47	0.141	1.040	0.893
58	35.98	0.155	1.054	0.874
59	36.95	0.137	0.849	0.815
60	43.66	0.133	0.749	0.691
61	45.78	0.104	0.508	0.508
62	38.48	0.164	1.024	0.835
63	39.99	0.132	0.830	0.751
64	37.78	0.176	1.109	0.846
65	39.46	0.140	1.034	0.895
66	34.77	0.181	1.193	0.889
67	37.85	0.119	0.526	0.580
68	36.53	0.141	0.914	0.831
69	38.37	0.102	0.497	0.541
70	34.50	0.196	1.233	0.925
71	36.75	0.138	0.869	0.818
72	45.21	0.111	0.580	0.564
73	38.88	0.152	1.015	0.839
74	43.42	0.082	0.423	0.489

Table A.4. Summary of analyzed experimental debris dam hydrodynamic values. (Continued)

75	44.14	0.131	0.703	0.657
76	45.26	0.111	0.577	0.562
77	36.05	0.153	1.055	0.880
78	34.28	0.202	1.378	0.994
79	37.22	0.135	0.821	0.814
80	40.16	0.130	0.810	0.759
81	44.42	0.125	0.648	0.603
82	39.87	0.133	0.844	0.759
83	41.02	0.123	0.678	0.652
84	35.54	0.166	1.134	0.891
85	37.14	0.136	0.831	0.820
86	40.30	0.129	0.791	0.751
87	42.08	0.115	0.532	0.517
88	44.65	0.119	0.639	0.605
89	42.17	0.142	0.951	0.816
90	43.52	0.135	0.747	0.681
91	39.56	0.139	0.972	0.847
92	40.53	0.128	0.725	0.687
93	34.07	0.204	1.446	1.029
94	37.12	0.138	0.835	0.821
95	42.95	0.136	0.791	0.710
96	38.59	0.160	1.030	0.838
97	40.96	0.124	0.703	0.672
98	41.56	0.148	1.070	0.896
99	44.04	0.131	0.689	0.641
100	38.64	0.161	1.020	0.829
101	38.34	0.164	1.026	0.836
102	41.69	0.118	0.641	0.620
103	38.18	0.167	1.105	0.881
104	40.10	0.131	0.796	0.743
105	36.76	0.201	1.233	0.892
106	39.74	0.136	0.894	0.785
107	38.30	0.165	1.054	0.848
108	41.49	0.120	0.662	0.649
109	38.75	0.154	1.070	0.876
110	41.33	0.121	0.657	0.631
111	40.87	0.126	0.758	0.719
112	40.83	0.126	0.762	0.723

Table A.4. Summary of analyzed experimental debris dam hydrodynamic values. (Continued)

113	40.62	0.128	0.746	0.698
114	42.64	0.102	0.544	0.547
115	40.21	0.130	0.817	0.768
116	41.36	0.120	0.657	0.631

Table A.5. Summary of analyzed experimental debris dam results; horizontal forces, moments, effective lever arms, and submerged projected areas.

Dam ID	$F_{h\,DEB}$ [N]	$F_{h\,CW}$ [N]	$M_{h\,DEB}$ [N-m]	$M_{h\,CW}$ [N-m]	r_{DEB} [m]	r_{CW} [m]	A_{sp} [m^2]
1	281.21	253.31	69.80	60.43	0.248	0.238	0.0938
2	135.41	121.17	29.89	21.41	0.221	0.177	0.0944
3	422.34	351.47	106.22	84.21	0.252	0.240	0.0960
4	339.46	277.24	97.45	66.23	0.287	0.239	0.1170
5	151.99	132.06	29.76	23.58	0.196	0.178	0.0847
6	448.31	405.49	118.35	94.95	0.264	0.236	0.1113
7	164.16	155.54	35.59	25.68	0.217	0.164	0.0835
8	125.52	99.32	29.93	18.73	0.238	0.190	0.0669
9	163.69	217.02	45.28	47.67	0.277	0.216	0.0976
10	151.26	101.28	33.58	18.79	0.222	0.188	0.1526
11	94.920	38.64	25.97	9.82	0.274	0.254	0.0743
12	88.180	27.73	26.45	5.36	0.300	0.196	0.1076
13	331.04	138.61	96.77	32.18	0.292	0.233	0.1248
14	121.96	50.64	20.23	9.95	0.166	0.201	0.0835
15	245.72	192.51	43.27	34.90	0.176	0.181	0.0829
16	188.20	80.58	51.16	19.28	0.272	0.233	0.1488
17	236.63	56.43	55.75	11.10	0.236	0.198	0.1726
18	44.130	23.38	9.71	4.70	0.220	0.208	0.0614
19	141.42	72.42	36.23	16.53	0.256	0.228	0.1044
20	81.650	54.30	17.73	10.78	0.217	0.198	0.0744
21	354.81	180.51	118.51	45.08	0.334	0.249	0.1343
22	106.14	75.15	22.95	17.10	0.216	0.227	0.0476
23	173.77	134.63	32.38	23.06	0.186	0.171	0.0735
24	248.96	79.70	81.13	18.77	0.326	0.240	0.1235
25	154.39	40.98	41.44	9.98	0.268	0.243	0.1356
26	178.75	68.99	59.92	15.36	0.335	0.214	0.1161
27	97.220	42.39	26.60	10.27	0.274	0.244	0.0818
28	119.25	26.65	46.47	5.25	0.390	0.199	0.1053
29	119.98	49.85	45.37	11.62	0.378	0.233	0.0787
30	170.32	42.35	50.87	10.78	0.299	0.254	0.0917
31	179.28	87.43	51.67	18.20	0.288	0.207	0.1309
32	323.30	178.16	101.61	38.30	0.314	0.213	0.0924
33	201.46	108.99	61.54	19.10	0.305	0.172	0.1262
34	76.230	38.90	18.31	7.79	0.240	0.203	0.0931
35	228.69	110.99	61.24	22.09	0.268	0.199	0.1260

Table A.5. Summary of analyzed experimental debris dam results; horizontal forces, moments, effective lever arms, and submerged projected areas. (Continued)

36	164.30	76.38	55.22	16.99	0.336	0.227	0.1121
37	52.06	27.64	10.51	7.18	0.202	0.275	0.0805
38	292.49	181.81	75.85	41.10	0.259	0.227	0.1443
39	484.55	255.02	162.80	56.56	0.336	0.222	0.2519
40	153.32	96.47	25.92	16.77	0.169	0.174	0.1023
41	131.00	103.00	25.75	19.86	0.197	0.193	0.1173
42	186.98	78.25	51.36	16.58	0.275	0.212	0.1424
43	175.84	111.96	43.27	23.57	0.246	0.205	0.1197
44	138.21	87.41	28.71	18.20	0.208	0.209	0.0850
45	272.01	238.58	67.12	54.61	0.247	0.229	0.0838
46	167.67	139.42	38.06	29.22	0.227	0.210	0.0829
47	500.11	438.69	163.44	140.52	0.327	0.320	0.0768
48	323.77	264.74	81.74	60.18	0.252	0.227	0.0925
49	173.94	121.95	47.15	28.64	0.271	0.235	0.1124
50	82.17	50.97	19.52	9.63	0.238	0.189	0.0765
51	223.11	186.50	63.08	42.88	0.283	0.231	0.0877
52	193.70	143.26	56.66	30.49	0.293	0.214	0.0952
53	281.56	257.65	72.64	56.97	0.258	0.221	0.0707
54	191.66	180.20	43.78	39.30	0.228	0.217	0.0606
55	307.48	251.34	80.44	56.14	0.262	0.224	0.0979
56	241.12	193.05	65.78	45.07	0.273	0.233	0.0625
57	225.35	159.48	59.28	34.85	0.263	0.219	0.1045
58	234.08	205.01	60.58	47.37	0.259	0.231	0.1065
59	259.22	163.91	67.80	30.92	0.262	0.188	0.1210
60	118.71	98.33	25.55	20.21	0.215	0.204	0.0742
61	60.85	47.67	12.36	8.91	0.203	0.186	0.0786
62	297.82	194.73	72.41	44.97	0.243	0.231	0.1073
63	181.67	131.14	51.29	27.90	0.282	0.212	0.0782
64	182.55	147.23	49.10	34.98	0.269	0.237	0.0815
65	121.35	94.33	31.29	23.07	0.258	0.243	0.0486
66	416.95	164.60	168.78	39.12	0.405	0.234	0.1348
67	172.47	64.09	36.11	13.53	0.209	0.203	0.1370
68	236.07	107.46	63.91	24.06	0.271	0.220	0.1266
69	133.03	56.50	25.45	8.94	0.191	0.157	0.0908
70	465.82	392.04	120.20	92.10	0.258	0.235	0.0874
71	246.50	220.87	51.29	42.50	0.208	0.192	0.0740

Table A.5. Summary of analyzed experimental debris dam results; horizontal forces, moments, effective lever arms, and submerged projected areas. (Continued)

72	108.42	73.25	27.23	12.34	0.251	0.163	0.0923
73	340.00	232.55	106.55	53.58	0.313	0.227	0.0879
74	114.78	56.07	26.16	6.02	0.228	0.107	0.1209
75	76.38	47.80	17.90	11.04	0.234	0.232	0.0732
76	66.16	30.98	17.71	6.70	0.268	0.218	0.0569
77	361.56	128.34	116.30	30.49	0.322	0.238	0.1273
78	384.31	188.72	144.12	48.30	0.375	0.254	0.1634
79	169.22	88.40	38.58	19.36	0.228	0.221	0.0762
80	258.22	70.75	82.69	16.14	0.320	0.225	0.1282
81	133.78	75.80	32.36	16.98	0.242	0.227	0.0832
82	152.65	135.50	41.00	28.28	0.269	0.211	0.0969
83	185.62	96.17	46.91	17.34	0.253	0.180	0.1489
84	367.63	240.66	112.67	54.15	0.306	0.226	0.1202
85	230.58	155.41	67.62	28.92	0.293	0.183	0.1388
86	148.01	118.30	35.48	23.64	0.240	0.200	0.0984
87	103.64	68.73	25.09	15.30	0.242	0.223	0.0983
88	98.74	69.59	19.88	15.35	0.201	0.222	0.0737
89	150.73	129.81	44.28	30.49	0.294	0.232	0.0741
90	147.98	99.86	34.61	19.95	0.234	0.205	0.0921
91	217.42	155.21	52.71	34.02	0.242	0.219	0.1037
92	156.10	111.84	30.87	22.32	0.198	0.199	0.0752
93	403.01	377.62	105.33	96.83	0.261	0.253	0.0724
94	216.05	156.52	49.97	29.25	0.231	0.185	0.1010
95	139.82	112.99	34.57	24.17	0.247	0.210	0.0617
96	250.31	194.14	68.35	45.20	0.273	0.233	0.0615
97	182.28	97.21	42.29	17.78	0.232	0.180	0.1180
98	154.98	147.62	39.52	33.95	0.255	0.229	0.0561
99	102.78	87.29	22.27	18.19	0.217	0.209	0.0629
100	136.35	122.15	38.93	27.34	0.286	0.224	0.0494
101	308.62	262.95	80.97	61.70	0.262	0.238	0.0938
102	118.88	105.14	24.08	19.08	0.203	0.187	0.0667
103	341.61	285.15	93.07	66.14	0.272	0.232	0.1152
104	230.49	170.99	55.14	34.68	0.239	0.201	0.0945
105	441.25	397.10	123.10	109.55	0.279	0.274	0.0880
106	228.87	200.67	59.67	41.37	0.261	0.206	0.1001
107	291.97	267.31	76.44	62.34	0.262	0.236	0.0939
108	132.44	117.50	27.10	20.71	0.205	0.177	0.0722

Table A.5. Summary of analyzed experimental debris dam results; horizontal forces, moments, effective lever arms, and submerged projected areas. (Continued)

109	298.31	241.32	84.58	58.32	0.284	0.237	0.0966
110	151.16	123.71	32.63	21.75	0.216	0.177	0.0761
111	185.02	136.19	35.36	22.90	0.191	0.170	0.0773
112	167.67	137.22	31.43	22.83	0.187	0.168	0.0708
113	183.97	147.30	45.09	26.15	0.245	0.171	0.1085
114	98.31	71.21	29.27	10.30	0.298	0.145	0.0963
115	191.95	167.38	49.50	33.32	0.258	0.195	0.0862
116	212.87	123.06	82.79	21.70	0.389	0.177	0.0910